symmetry

Article

Numerical and Machine Learning Approach for Fe_3O_4-Au/Blood Hybrid Nanofluid Flow in a Melting/Non-Melting Heat Transfer Surface with Entropy Generation

Shaik Jakeer [1], Sathishkumar Veerappampalayam Easwaramoorthy [2,*], Seethi Reddy Reddisekhar Reddy [3] and Hayath Thameem Basha [4]

1 Center for Computational Modeling, Chennai Institute of Technology, Chennai 600069, India; shaikjakeer@citchennai.net
2 Department of Software Engineering, Jeonbuk National University, Jeonju 54896, Republic of Korea
3 Department of Mathematics, Koneru Lakshmaiah Education Foundation, Bowrampet, Hyderabad 500043, India; seethireddy@klh.edu.in
4 Department of Mathematical Sciences, Ulsan National Institute of Science and Technology, Ulsan 44919, Republic of Korea; basha666@unist.ac.kr
* Correspondence: sathish@jbnu.ac.kr

Abstract: The physiological system loses thermal energy to nearby cells via the bloodstream. Such energy loss can result in sudden death, severe hypothermia, anemia, high or low blood pressure, and heart surgery. Gold and iron oxide nanoparticles are significant in cancer treatment. Thus, there is a growing interest among biomedical engineers and clinicians in the study of entropy production as a means of quantifying energy dissipation in biological systems. The present study provides a novel implementation of an intelligent numerical computing solver based on an MLP feed-forward backpropagation ANN with the Levenberg–Marquard algorithm to interpret the Cattaneo–Christov heat flux model and demonstrate the effect of entropy production and melting heat transfer on the ferrohydrodynamic flow of the Fe_3O_4-Au/blood Powell–Eyring hybrid nanofluid. Similarity transformation studies symmetry and simplifies PDEs to ODEs. The MATLAB program bvp4c is used to solve the nonlinear coupled ordinary differential equations. Graphs illustrate the impact of a wide range of physical factors on variables, including velocity, temperature, entropy generation, local skin friction coefficient, and heat transfer rate. The artificial neural network model engages in a process of data selection, network construction, training, and evaluation through the use of mean square error. The ferromagnetic parameter, porosity parameter, distance from origin to magnetic dipole, inertia coefficient, dimensionless Curie temperature ratio, fluid parameters, Eckert number, thermal radiation, heat source, thermal relaxation parameter, and latent heat of the fluid parameter are taken as input data, and the skin friction coefficient and heat transfer rate are taken as output data. A total of sixty data collections were used for the purpose of testing, certifying, and training the ANN model. From the results, it is found that the fluid temperature declines when the thermal relaxation parameter is improved. The latent heat of the fluid parameter impacts the entropy generation and Bejan number. There is a less significant impact on the heat transfer rate of the hybrid nanofluid over the sheet on the melting heat transfer parameter.

Keywords: Fe_3O_4-Au/blood Powell–Eyring hybrid nanofluid; magnetic dipole; Cattaneo–Christov heat flux; entropy generation and melting/non-melting heat transfer

check for updates

Citation: Jakeer, S.; Easwaramoorthy, S.V.; Reddy, S.R.R.; Basha, H.T. Numerical and Machine Learning Approach for Fe_3O_4-Au/Blood Hybrid Nanofluid Flow in a Melting/Non-Melting Heat Transfer Surface with Entropy Generation. *Symmetry* **2023**, *15*, 1503. https://doi.org/10.3390/sym15081503

Academic Editors: Liaqat Ali, Bagh Ali, Dumitru Vieru and Nehad Ali Shah

Received: 26 June 2023
Revised: 19 July 2023
Accepted: 25 July 2023
Published: 28 July 2023

1. Introduction

Computer simulations and physical–mathematical models of non-Newtonian fluids have received a lot of interest in recent years. Examples of non-Newtonian fluid subcategories include grease, medicines, symmetry in drug delivery, industrial lubricants, gels, chemicals (polymers, paints, and plastics), and foodstuffs (honey, yogurt, and ketchup), as well as ecological systems including highly concentrated sediments, oil spills, mudflows, and pollution discharge. The drawing of plastic films, petroleum purification, food technology, chemical materials, symmetric coating production, insulating materials, aerospace, metal spinning operations, and paper production are just a few examples of the many industries that use non-Newtonian fluids. Due to their fundamental characteristics, the traditional Navier–Stokes equations for the viscous model are insufficient for non-Newtonian fluids. To precisely describe the properties of non-Newtonian fluids, researchers offered numerous nonlinear mathematical models, including the Casson, Maxwell, Sisko, Bingham plastic, Carreau–Yasuda, Eyring–Powell, Jeffrey fluid, Williamson, Brinkman type, and Oldroyd-B models. Instead of using empirical relationships, the kinetic theory of gases is used to determine the constitutive equation for the Eyring–Powell liquid [1] model of a non-Newtonian fluid. Therefore, researchers have started to use the Powell–Eyring fluid model with greater frequency. The Eyring–Powell fluid model is crucial for industrial processes that are both natural and geophysical, such as those that include underground energy transfer, thermal insulation, and pollution abatement. Asha and Sunitha [2] studied the effects of Joule heating and magnetohydrodynamics on the peristaltic blood flow of Eyring–Powell nanofluid in a non-uniform channel. Jafarimoghaddam [3] used PST and PHF to examine the magnetohydrodynamic flow caused by a nonlinearly stretched sheet acting on non-Newtonian Eyring–Powell fluids within a porous Darcy–Forchheimer medium. Patil et al. [4] explored the unstable MHD flow of a Powell–Eyring nanofluid approaching a stagnation point through a convectively warmed extended surface in the presence of a chemical reaction with thermal radiation. Farooq et al. [5] investigated entropy in convective heat transfer Powell–Eyring magnesium–blood nanofluid convection across a linearly stretched surface at the stagnation point.

The first law of thermodynamics deals with the quantity rather than the quality of energy and the interchangeability of its many forms. Engineers are primarily concerned with minimizing the rate and extent to which energy is degraded in a practical setting. Despite this, the quality of power is doomed to diminish (second principle of thermodynamics), and the rate at which this happens is quantified by entropy. To reduce this loss in energy quality (the exergy), examining how entropy is generated across the flow field is essential. Numerous researchers have studied the topic of minimizing entropy creation during fluid flow with heat transfer. Entropy is a unit of measure for the quantity of energy that cannot be used for work in thermodynamics. Heat exchanger pumps and electronic cooling systems are two examples of entropy creation in use. Researchers and engineers are extremely interested in developing strategies to prevent the waste of valuable energy, particularly in thermodynamical systems, because energy loss may cause significant disruption. Radiation, conduction, convection, and evaporation are the methods through which heat is transferred in the human body. Additionally, heat is transferred through the circulatory system, where heat is lost to surrounding tissues by pulmonary blood flow. The human body loses heat through conduction and radiation when temperatures are below 20 °C. Entropy generation is essential in preventing the waste of usable energy in order to control this condition. Bejan [6] used entropy optimization to demonstrate the characteristics of thermal conductivity in fluids. Jakeer and Reddy [7] investigated the entropy production in a variable magnetic field and the magnetohydrodynamic stagnation point flow of an Eyring–Powell hybrid dusty nanofluid. They declared that the nature of entropy generation (N_G) and Bejan number (Be) on the Brinkman number are completely contradictory (Br).

The magnetic field plays a crucial part in controlling the properties of fluid motion, which is essential for symmetric biomedical devices, high-temperature plasma, cooling of atomic reactors, symmetric magnetohydrodynamics generators, hyperthermia, and other applications [8]. Recently, efforts have been undertaken to develop a mathematical model of biomagnetic fluids by adapting the field of ferrohydrodynamics (FHD), which investigates the mechanics of fluid motion as it is affected by strong magnetic polarization forces. The term "ferrofluid" refers to a colloidal dispersion of magnetic particles in a liquid. The thermal Brownian motion of the colloidal particles and the conditions under which each particle is permanently magnetized considerably influence the characteristics of a ferrofluid. The expansion of the efficacious magnetic force, which significantly affects fluid temperature, gives ferrofluids their distinctive fluid features. The first ferrofluid synthesis was discovered in 1965 as a result of Papell's creative research [9]. In the medical area, magnetic nanoparticles in bodily fluids such as lymph fluid and blood are employed for medication transfer at the specific afflicted site, allowing for novel cancer therapy approaches and inducing hyperthermia, and magneto-nanofluids are useful for directing the movement of particles up the bloodstream to a tumor using magnets [8,10,11]. Nasir et al. [12] explored the effect of nonlinear thermal radiation on the ferrohydrodynamic flow of a SiO_2 + TiO_2 + Al_2O_3/H_2O hybrid nanofluid on a stretched sheet. Results showed that maximum radiation values and minimum ferromagnetic parameter levels result in extraordinarily high heat transfer rates.

Heat transfer is important in many industrial and technical processes, such as combustors, axial blade compressors, fuel cells, heat exchangers, symmetric microelectronic board circuits, gas turbine blades, computer processors, and hybrid engines. Madhura et al. [13] investigated a novel solution for studying heat and mass transfer in a nanofluid over a moving/stationary vertical plate in a porous medium. The free convection flow, heat, and mass transfer of fractional nanofluids made of several base fluids (water, sodium alginate, and ethylene glycol) suspended with copper nanoparticles via an endless vertical plate with radiation effect were studied by Madhura et al. [14]. Saleem et al. [15] used the finite volume approach and the Boussinesq approximation for buoyancy effects to study the numerical analysis of steady-state laminar 2D rarefied gaseous flow in a partly heated square two-sided wavy cavity with internal heat production. Kheioon et al. [16] examined the influence of vacuum pressure on convection and radiation heat transfer rates from a solid cylindrical rod inside a vacuum-sealed tank. The natural convective Cu-water nanofluid flow in a l-shaped cavity with a fluctuating temperature was studied by Saleem et al. [17]. The thermal behavior and entropy production of a moving, wet porous fin made of linear functionally graded material (FGM) under convective–radiative heat transmission were studied by Keerthi et al. [18]. The novelty of the present study is the use of a non-Fourier heat flux model to look at the melting heat transfer properties of a Powell–Eyring hybrid nanofluid in a ferrohydrodynamic flow. Blood is used as a base fluid; iron oxide (Fe_3O_4) and gold (Au) nanoparticles are added to it. The generation of entropy in biological processes is also evidently employed to treat cancerous tissues and enhance the performance of medical equipment. Furthermore, the aforementioned research revealed that no investigations have been conducted on the entropy production and melting heat transfer during the ferrohydrodynamic flow of iron oxide (Fe_3O_4) and gold (Au)/blood Powell–Eyring hybrid nanofluid using a non-Fourier heat flux model. The consequences of Joule heating, viscous dissipation, and the more realistic characteristic of melting heat transfer are adopted to examine heat transmission.

2. Mathematical Formulation

The present analysis discusses the steady 2D laminar, incompressible ferrohydrodynamic flow of a Powell–Eyring hybrid nanofluid made of Fe_3O_4 and gold flowing across a melting/non-melting heat transfer surface. Figure 1 depicts the schematic diagram of the flow problem. It is considered that the surface is being stretched along the x-axis with the velocity $U_w = bx$, where $b > 0$ is the stretching case. A magnetic dipole is positioned at a distance a_1 from the sheet, with its center located on the y-axis. The magnetic field generated by the dipole points in the positive x-direction and is strong enough to saturate the ferrofluid. It is assumed that T_∞ is the ambient fluid temperature and that T_c is the melting surface temperature. A non-Darcy porous medium, uniform heat source/sink, viscous dissipation, and Cattaneo–Christov heat flux are also considered. Table 1 presents the thermophysical options for the Flow system. Assuming the given conditions and utilizing the Boussinesq approximation, it is possible to express the governing equations as follows [19,20]:

$$\frac{\partial u}{\partial x}+\frac{\partial v}{\partial y}=0 \tag{1}$$

$$u\frac{\partial u}{\partial x}+v\frac{\partial u}{\partial y}=\left(v_{hnf}+\frac{1}{\rho_{hnf}\beta c}\right)\frac{\partial^2 u}{\partial y^2}-\frac{1}{2\rho_{hnf}\beta c^3}\left(\frac{\partial u}{\partial y}\right)^2\left(\frac{\partial^2 u}{\partial y^2}\right)+\frac{m_p}{\rho_{hnf}}M\frac{\partial H}{\partial x}-\frac{v_{hnf}}{k'}u-\frac{F^*}{\sqrt{k'}}u^2, \tag{2}$$

$$\begin{aligned}&u\frac{\partial T}{\partial x}+v\frac{\partial T}{\partial y}+\frac{1}{(\rho c_p)_{hnf}}m_pT\frac{\partial M}{\partial T}\left(u\frac{\partial H}{\partial x}+v\frac{\partial H}{\partial y}\right)+\lambda_T\left[u\left(\frac{\partial u}{\partial x}\frac{\partial T}{\partial x}+\frac{\partial v}{\partial x}\frac{\partial T}{\partial y}\right)+v\left(\frac{\partial u}{\partial y}\frac{\partial T}{\partial x}+\frac{\partial v}{\partial y}\frac{\partial T}{\partial y}\right)\right.\\&\left.+u^2\frac{\partial^2 T}{\partial x^2}+v^2\frac{\partial^2 T}{\partial y^2}+2uv\frac{\partial^2 T}{\partial x\partial y}\right]=\alpha_{hnf}\frac{\partial^2 T}{\partial y^2}-\frac{1}{(\rho c_p)_{hnf}6\beta c^3}\left(\frac{\partial u}{\partial y}\right)^4+\frac{1}{(\rho c_p)_{hnf}}\left(\mu_{hnf}+\frac{1}{\beta c}\right)\left(\frac{\partial u}{\partial y}\right)^2\\&+\frac{1}{(\rho c_p)_{hnf}}\frac{16\sigma^* T_c^3}{3k^*}\frac{\partial^2 T}{\partial y^2}+\frac{Q_0}{(\rho c_p)_{hnf}}(T-T_c)\end{aligned} \tag{3}$$

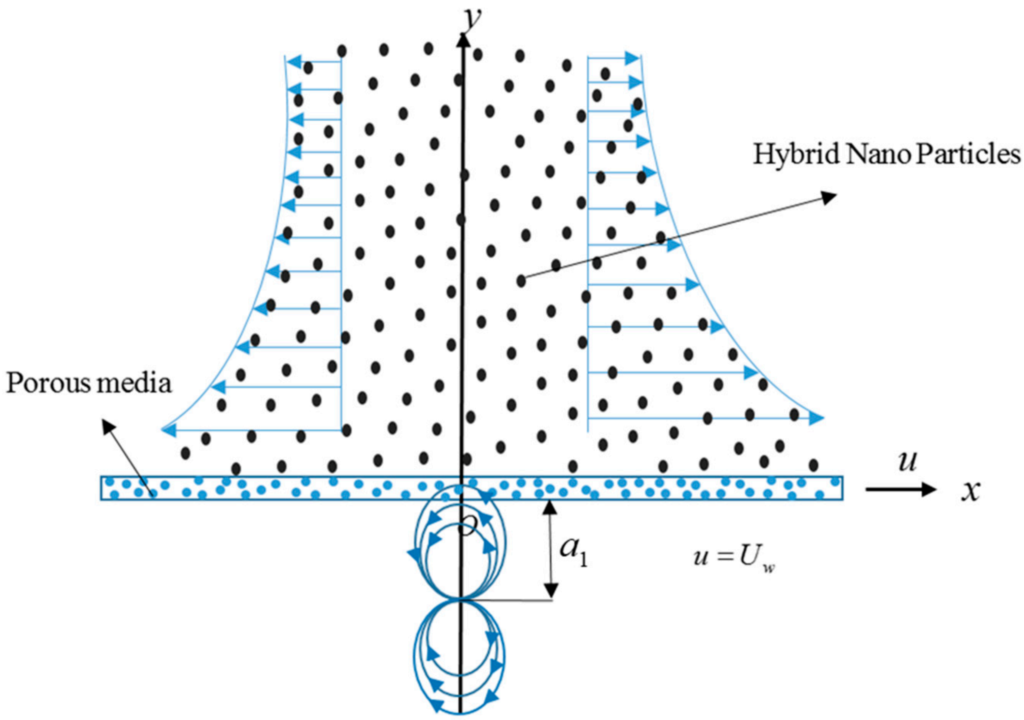

Figure 1. Coordinate system and model.

Table 1. Density (ρ), specific heat (C_p), and thermal conductivity (k) of magnetite, silver, and base fluid.

Physical Properties	ρ $(\mathrm{kg/m^3})$	c_p (J/kg K)	k (W/m K)	Pr
Blood	1050	3617	0.52	21
Fe_3O_4	5200	670	6	-
Au	19,300	129	318	-

The boundary conditions are [21]

$$\begin{array}{l} u=u_w,\ T=T_c,\ \text{at}\quad y=0,\\ u\to 0,\ T\to T_\infty\ \text{as}\quad y\to\infty, \end{array} \tag{4}$$

and

$$k_{hnf}\left(\frac{\partial T}{\partial y}\right)_{y=0}=\rho_{hnf}(\lambda+c_s[T_c-T_s])v(x,0). \tag{5}$$

According to a description of the magnetic scalar potential,

$$\Theta = \frac{\gamma^*}{2\pi}\left(\frac{x}{x^2 + (y + a_1)^2}\right) \tag{6}$$

Here γ^* and H exhibit the strength and elements of a magnetic field and can be expressed as

$$H_x = -\frac{\partial\Theta}{\partial x} = \frac{\gamma^*}{2\pi}\left(\frac{x^2 - (y + a_1)^2}{\left(x^2 + (y + a_1)^2\right)^2}\right) \tag{7}$$

$$H_y = -\frac{\partial\Theta}{\partial y} = \frac{\gamma^*}{2\pi}\left(\frac{2x(y + a_1)}{\left(x^2 + (y + a_1)^2\right)^2}\right) \tag{8}$$

$$H = \left(\left[\frac{\partial\Theta}{\partial x}\right]^2 + \left[\frac{\partial\Theta}{\partial y}\right]^2\right)^{\frac{1}{2}} \tag{9}$$

Following the expansion in powers of x and the retention of terms up to order x^2,

$$\frac{\partial H}{\partial x} = -\frac{\gamma^*}{2\pi}\left(\frac{2x}{(y + a_1)^4}\right), \tag{10}$$

$$\frac{\partial H}{\partial y} = \frac{\gamma^*}{2\pi}\left(\frac{4x^2}{(y + a_1)^5} - \frac{2}{(y + a_1)^3}\right), \tag{11}$$

Therefore, the modification of M through T can be expressed as

$$M = K^*(T_c - T) \tag{12}$$

where T_c is the Curie temperature and K^* is a pyromagnetic coefficient.

The thermophysical properties of hybrid nanofluids are furnished by [22]

$$\left.\begin{array}{l}
\frac{\mu_{hnf}}{\mu_f} = \frac{1}{(1-\phi_{Fe_3O_4})^{2.5}(1-\phi_{Au})^{2.5}}, \alpha_{hnf} = \frac{k_{hnf}}{(\rho C_p)_{hnf}}, \\
\frac{\rho_{hnf}}{\rho_f} = (1 - \phi_{Au})\left((1 - \phi_{Fe_3O_4}) + \phi_{Fe_3O_4}\frac{\rho_{Fe_3O_4}}{\rho_f}\right) + \phi_{Au}\frac{\rho_{Au}}{\rho_f}, \\
\frac{(\rho C_p)_{hnf}}{(\rho C_p)_f} = (1 - \phi_{Au})\left((1 - \phi_{Fe_3O_4}) + \phi_{Fe_3O_4}\frac{(\rho C_p)_{Fe_3O_4}}{(\rho C_p)_f}\right) + \phi_{Au}\frac{(\rho C_p)_{Au}}{(\rho C_p)_f}, \\
\frac{k_{hnf}}{k_{bf}} = \frac{(1+2\phi_{Au})k_{Au}+2(1-\phi_{Au})k_{bf}}{(1-\phi_{Au})k_{Au}+(2+\phi_{Au})k_{bf}}, \text{where } \frac{k_{bf}}{k_f} = \frac{(1+2\phi_{Fe_3O_4})k_{Fe_3O_4}+2(1-\phi_{Fe_3O_4})k_f}{(1-\phi_{Fe_3O_4})k_{Fe_3O_4}+(2+\phi_{Fe_3O_4})k_f}.
\end{array}\right\} \tag{13}$$

where μ_{hnf} is the viscosity of hybrid nanofluid, ϕ is the nanoparticle volume fraction, and ρ_f and k_f are the thermal conductivities of fluid and nanoparticles, respectively.

The non-dimensional variables are

$$\psi(\zeta,\eta) = v_f\zeta f(\eta), \ \ \theta(\zeta,\eta) = \frac{T_c - T}{T_c - T_\infty} = \theta_1(\eta) + \zeta^2\theta_2(\eta) \tag{14}$$

The dimensionless coordinates η and ζ are defined as

$$\eta = \left(\frac{U_0}{v_f}\right)^{0.5} y, \ \zeta = \left(\frac{U_0}{v_f}\right)^{0.5} x \tag{15}$$

The velocity components are

$$u = \frac{\partial \psi}{\partial y}, v = -\frac{\partial \psi}{\partial x}$$

By using Equations (14) and (15), Equations (2)–(5) are reduced as follows:

$$\left(\frac{\mu_{hnf}}{\mu_f} + \in\right) f''' - \frac{\rho_{hnf}}{\rho_f}\left[f'^2 - f'' f + F_s f'^2\right] - \frac{2\beta_f}{(\eta+\alpha)^4}\theta_1 - \delta \in f''^2 f''' - K\frac{\mu_{hnf}}{\mu_f} f' = 0, \tag{16}$$

$$\begin{aligned} &\tfrac{1}{Pr}\left(\tfrac{k_{hnf}}{k_f} + \tfrac{4}{3}R\right)\theta_1'' + \frac{(\rho c_p)_{hnf}}{(\rho c_p)_f} f\theta_1' + \tfrac{2\lambda\beta_f}{\mathrm{Pr}}(\theta_1 - \varepsilon)\tfrac{f}{(\eta+\alpha)^3} + Q\,\theta_1 \\ &+Ec\left[\left(\tfrac{\mu_{hnf}}{\mu_f} + \in\right) f''^2 - \tfrac{\delta\in}{3} f''^4\right] - \beta_e\left(f f'\theta_1' + f^2\theta_1''\right) = 0, \end{aligned} \tag{17}$$

$$\begin{aligned} &\tfrac{1}{Pr}\left(\tfrac{k_{hnf}}{k_f} + \tfrac{4}{3}R\right)\theta_2'' - \frac{(\rho c_p)_{hnf}}{(\rho c_p)_f}\left(2f'\theta_2 - f\theta_2'\right) - \tfrac{2\lambda\beta_t}{\mathrm{Pr}}(\theta_1 - \varepsilon)\left(\tfrac{f'}{(\eta+\alpha)^4} + \tfrac{2f}{(\eta+\alpha)^5}\right) \\ &-\beta_e\left(4f'^2\theta_2 + f^2\theta_2'' - 2ff''\theta_2 - 3ff'\theta_2'\right) + \tfrac{2\lambda\beta_f}{\mathrm{Pr}}\tfrac{f\theta_2}{(\eta+\alpha)^3} + Q\,\theta_2 = 0, \end{aligned} \tag{18}$$

With boundary conditions

$$\left.\begin{aligned} &f'(0) = 1, Pr\tfrac{\rho_{hnf}}{\rho_f} f(0) + \tfrac{k_{hnf}}{k_f} Me\,\theta_1'(0) = 0, \quad \theta_1(0) = 0, \theta_2(0) = 0, \\ &f'(\infty) = 0,\ \theta_1(\infty) = 1,\ \theta_2(\infty) = 0. \end{aligned}\right\} \tag{19}$$

where $K = \frac{\nu_f}{k' U_0}$, $F_s = \frac{u_w F^*}{U_0\sqrt{k'}}$, $Pr = \frac{\mu_f (c_p)_f}{k_f}$, $\beta_e = \lambda_T U_0$, $Ec = \frac{u_w^2}{(c_p)_f (T_\infty - T_c)}$, $\lambda = \frac{U_0 \mu_f^2}{\rho_f k_f (T_c - T_\infty)}$, $R = \frac{4\sigma^* T_\infty^3}{3k^* k_f}$, $Q = \frac{Q_0}{U_0 (\rho c_p)_f}$, $Me = \frac{(c_p)_f (T_\infty - T_c)}{(\lambda + c_s[T_c - T_s])}$, $\alpha = \sqrt{\frac{U_0}{\nu_f}} a$, $\beta_f = \frac{\gamma m_p K^*}{2\pi\rho_f \nu_f^2}(T_c - T_\infty)$, $\varepsilon = \frac{T_c}{T_c - T_\infty}$, $\in = \frac{1}{\beta c \mu_f}$, and $\delta = \frac{u_0^3 x^2}{2c^2 \nu_f}$.

Near the wall ($\eta = 0$), the skin friction factor and rate of heat transfer are

$$\begin{aligned} \tau_w &= \left[\mu_{hnf} + \tfrac{1}{\beta c}\right]\tfrac{\partial u}{\partial y} - \tfrac{1}{6\beta c^3}\left(\tfrac{\partial u}{\partial y}\right)^3 \\ q_w &= -k_{hnf}\left[1 + \tfrac{16\sigma^* T_\infty^3}{3k^* k_f}\right]\left(\tfrac{\partial T}{\partial y}\right) \end{aligned}$$

$$\left.\begin{aligned} &C_f Re_x^{1/2}/2 = \left(\tfrac{\mu_{hnf}}{\mu_f} + \in\right) f''(0) - \tfrac{\delta\in}{3}\left(f''(0)\right)^3, \\ &\mathrm{Nu}_x Re_x^{-1/2} = -\left(\tfrac{k_{hnf}}{k_f} + \tfrac{4}{3}R\right)\theta'(0), \end{aligned}\right\} \tag{20}$$

3. Modeling of Entropy

The volumetric entropy in dimensional form is

$$\begin{aligned} S_G = &\tfrac{1}{T_\infty^2}\left(k_{hnf} + \tfrac{16\sigma^* T_\infty^3}{3k^*}\right)\left(\tfrac{\partial T}{\partial y}\right)^2 - \tfrac{m_p T}{T_\infty}\tfrac{\partial M}{\partial T}\left(u\tfrac{\partial H}{\partial x} + v\tfrac{\partial H}{\partial y}\right) + \tfrac{1}{T_\infty}\left(\mu_{hnf} + \tfrac{1}{\beta c}\right)\left(\tfrac{\partial u}{\partial y}\right)^2 \\ &-\tfrac{1}{T_\infty}\left(\tfrac{1}{6\beta c^3}\right)\left(\tfrac{\partial u}{\partial y}\right)^4 + \tfrac{\mu_{hnf}}{k' T_\infty} u^2 \end{aligned} \tag{21}$$

By applying Equations (14) and (15) in Equation (21), the converted equation is

$$\begin{aligned} N_G = &\alpha_1\left(\tfrac{k_{hnf}}{k_f} + \tfrac{4}{3}R\right)\theta_1'^2 + 2\lambda\beta_f(\theta_1 - \varepsilon)\tfrac{f}{(\eta+\alpha_1)^3} \\ &+Br\left[\left(\tfrac{\mu_{hnf}}{\mu_f} + \in\right) f''^2 - \tfrac{\in\delta}{3} f''^4\right] + \tfrac{\mu_{hnf}}{\mu_f} Br\,K\,f'^2 \end{aligned} \tag{22}$$

where $\alpha_1 = \frac{\Delta T}{T_\infty}$ is the dimensionless ratio variable, $N_G = \frac{S_G \nu_f T_\infty}{k_f U_0 \Delta T}$ is the local entropy generation, and $Br = \frac{\mu_f {u_w}^2}{k_f \Delta T}$ is the Brinkman number.

The Bejan number (Be) is as follows:

$$Be = \frac{\text{Heat transfer irreversibility}}{\text{Total entropy genertion}}$$

$$Be = \frac{\left(\frac{k_{hnf}}{k_f} + \frac{4}{3}R\right)\alpha_1{}^* {\theta_1{}'}^2 + 2\lambda\beta_f\left(\frac{f\theta_1}{(\eta+\alpha_1)^3}\right)}{\left(\begin{array}{c} \alpha_1\left(\frac{k_{hnf}}{k_f} + \frac{4}{3}R\right)\theta_1'^2 + 2\lambda\beta_f(\theta_1 - \varepsilon)\frac{f}{(\eta+\alpha_1)^3} \\ +Br\left[\left(\frac{\mu_{hnf}}{\mu_f} + \in\right)f''2 - \frac{\in\delta}{3}f''4\right] + \frac{\mu_{hnf}}{\mu_f}Br\,K\,{f'}^2 \end{array}\right)} \tag{23}$$

4. Numerical Method

The set of higher-order nonlinear differential Equations (16)–(19) has been reduced to first-order equations by using the following process:

$$f = y_1,\ f\prime = y_2,\ f'' = y_3,\ \theta_1 = y_4,\ \theta_1\prime = y_5,\ \theta_2 = y_6,\ \theta_2\prime = y_7 \tag{24}$$

$$y_3\prime = \left(\left(\frac{\mu_{hnf}}{\mu_f} + \in\right) - \delta \in {y_3}^2\right)^{-1}\left(\frac{\rho_{hnf}}{\rho_f}\left[{y_2}^2 - y_3 y_1 + F_s {y_2}^2\right] + \frac{2\beta_f}{(\eta+\alpha)^4}y_4 + K\frac{\mu_{hnf}}{\mu_f}y_2\right) \tag{25}$$

$$y_5\prime = \frac{1}{\left(\frac{1}{Pr}\left(\frac{k_{hnf}}{k_f} + \frac{4}{3}R\right) - \beta_e {y_1}^2\right)}\left(\begin{array}{c} -\frac{(\rho c_p)_{hnf}}{(\rho c_p)_f}y_1 y_5 - \frac{2\lambda\beta_f}{\mathrm{Pr}}(y_4 - \varepsilon)\frac{y_1}{(\eta+\alpha)^3} - Q\,y_4 \\ -Ec\left[\left(\frac{\mu_{hnf}}{\mu_f} + \in\right){y_3}^2 - \frac{\delta\in}{3}{y_3}^4\right] + \beta_e y_1 y_2 y_5 \end{array}\right) \tag{26}$$

$$y_7\prime = \frac{1}{\left(\frac{1}{Pr}\left(\frac{k_{hnf}}{k_f} + \frac{4}{3}R\right) - \beta_e {y_1}^2\right)}\left(\begin{array}{c} +\frac{(\rho c_p)_{hnf}}{(\rho c_p)_f}(2y_1 y_6 - y_1 y_7) + \frac{2\lambda\beta_t}{\mathrm{Pr}}(y_4 - \varepsilon)\left(\frac{y_2}{(\eta+\alpha)^4} + \frac{2y_1}{(\eta+\alpha)^5}\right) \\ +\beta_e\left(4{y_2}^2 y_6 - 2y_1 y_3 y_6 - 3y_1 y_2 y_7\right) - \frac{2\lambda\beta_f}{\mathrm{Pr}}\frac{f y_6}{(\eta+\alpha)^3} - Q\,y_6 \end{array}\right) \tag{27}$$

With boundary conditions

$$\left.\begin{array}{c} y_2(0) = 1,\ Pr\frac{\rho_{hnf}}{\rho_f}y_1(0) + \frac{k_{hnf}}{k_f}Me\,y_5(0) = 0,\quad y_4(0) = 0,\ y_6(0) = 0, \\ y_2(\eta_\infty) = 0,\ y_4(\eta_\infty) = 1,\ y_6(\eta_\infty) = 0. \end{array}\right\} \tag{28}$$

Selecting a relatively small grade of η_∞ is a crucial component of bvp4c [23]. In this study, the step size is h = 0.001 and the error tolerance is 10^{-8}.

5. ANN Modeling

The artificial neural network is a contemporary computer systems approach that is based on the concept of the human brain functioning as a network of interconnected neural cells. This phenomenon has been observed to emulate the development of neural networks within the human brain. This model exhibits comparable performance to the human brain with regard to optimization, clustering, learning, classification, prediction, and generalization.

The following phrases outline the primary benefits of utilizing the artificial neural network (ANN) methodology:

- The ANN has demonstrated impressive performance and efficiency even when deployed on a limited hardware infrastructure.

- The use of ANN surprisingly simplifies the intricate process of class-distributed mapping.
- The input vector determines the appropriate results in the training set.
- The weights that signify the results are acquired through iterative training.

The implementation of a training rule and the linking of neurons result in a variety of architectures. Most often, the layers result from the neurons' tight interactions. Three distinct layers make up the ANN technique: input, hidden, and output. The information sent in from the outside world is received by these layers, processed, and then sent back via the ANN. Information obtained by the input layer is sent to the hidden layer neurons without being altered by the input layer's processing components. It is crucial to note that the weights, connection lines, and connecting neurons perform the information translation. The system maintains a database for ANN training, where input values and weights are saved. The construction of an ANN is guided by the utilization of data, which takes into account various factors such as determining the optimal number of layers and hidden neurons.

The multi-layer perceptron architecture-based feed-forward neural network (FFNN) has gained widespread popularity and is currently considered a highly intriguing ANN model. Compared to the backpropagation method, alternative approaches for training feed-forward neural networks exhibit lower levels of efficiency. The backpropagation algorithm can modify individual neurons' weights during the computation of the network's output error. This modification is uniformly applied across all neurons with the aim of reducing the output error.

The subsequent expression represents the net input of the j^{th} hidden neuron, as depicted in Figure 2: $y_j(x) = \sum_{i=1}^{l} W1_{ji} x_i + a_j$.

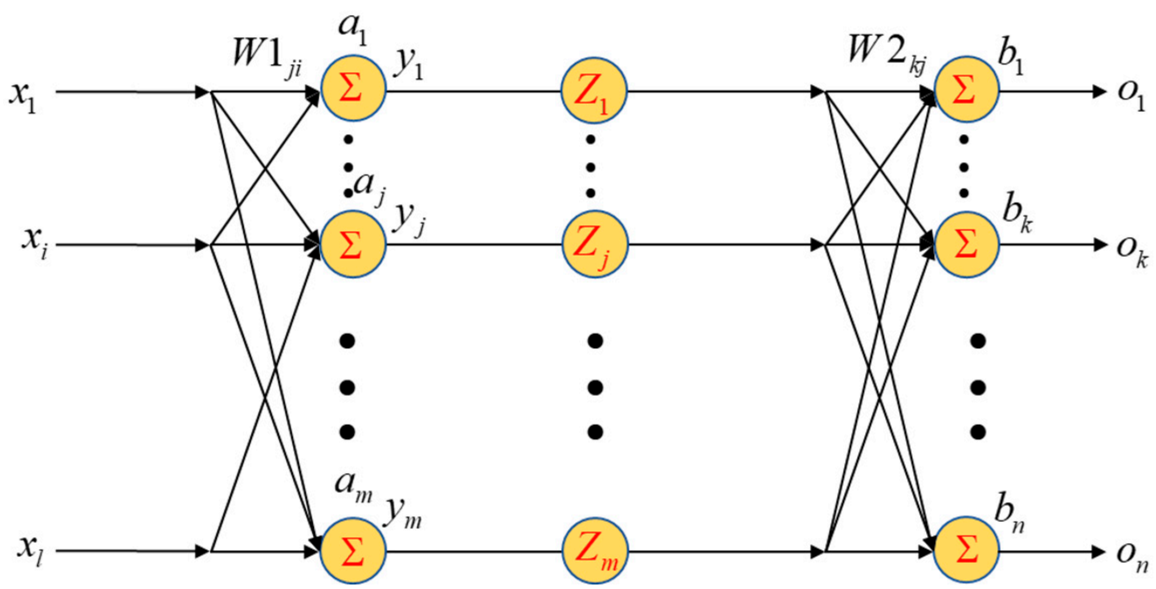

Figure 2. Diagrammatic representation of neural network backpropagation.

The input layer's i^{th} node is symbolized as x_i, while the hidden layer's j^{th} node is denoted as a_j. The weight connecting x_i and a_j is expressed as $W1_{ji}$.

The j^{th} hidden node's output is denoted in the following manner:

$$z_j(x) = \frac{1}{1 + e^{-y_j(x)}},$$

The k^{th} node of the output layer is denoted in the following manner:

$$o_k(x) = \sum_{j=1}^{m} W2_{kj} z_j + b_k$$

The weight $W2_{kj}$ serves as a means of connection between the k^{th} node of the output layer and the j^{th} node of the hidden layer. Additionally, the term b_k represents the bias associated with the k^{th} node of the output layer.

The present study involves the measurement of skin friction and heat transfer rates for representative samples of ANN output nodes, as illustrated in Figure 3. The parameters β_f, K, α, δ, F_s, ε, $\in$, Ec, R, Q, β_e and λ are estimated for the samples of input nodes. A trial-and-error approach is used to determine the hidden layer's node count depending on the number of epochs needed to train the network, avoid input parameter over- or under-setting, and ensure convergence of the learning process. Following such repeated processes, it was discovered that the convergence criteria employed were the introduction of one hidden layer with five neurons in order to reduce the disparity between the anticipated values of C_f and Nu. A total of sixty data collections were used for the purpose of testing, validating, and training the ANN model. Out of the total amount of data, 70% was utilized for training, 15% for validation, and the remaining 15% was used to test the model's predictions. The results of the skin friction coefficient and heat transfer rate in the training, validation, and test sets of the ANN model are shown in Figures 4 and 5. The ANN models are given everything they need to simulate the complex interaction between input and output variables. The results of the ANN model impressively match the values obtained by computation.

The process of determining the appropriate number of nodes in the hidden layer involves the utilization of trial and error. This is done by considering the number of epochs required to train the network, preventing the occurrence of over- or under-setting of input parameters, and guaranteeing the convergence of the learning process. Through iterative procedures, it was determined that the convergence criteria utilized involved the incorporation of a single hidden layer containing five neurons, with the aim of minimizing the discrepancy between the predicted values of Cf and Nu. Seventy percent of the entire dataset was allocated for training purposes, while 15% was reserved for validation and another 15% was utilized for testing the model's predictions. Figures 4 and 5 depict the outcomes of the skin friction coefficient and heat transfer rate in the training, validation, and test sets of the ANN model. The provided elements equip artificial neural network models with the necessary components to replicate intricate relationships between input and output variables. The outcomes of the ANN model exhibit a remarkable level of concurrence with the figures derived through computation. The skin friction coefficient and heat transfer rate are important parameters that contribute significantly to the benefits of the ferromagnetic parameter $\left(\beta_f = 1, 1.5, 2, 2.5\right)$, porosity parameter $(K = 0.7, 0.9, 1.1, 1.3)$, distance from origin to magnetic dipole $(\alpha = 1.4, 1.8, 2.2, 2.6)$, $(\delta = 0.1, 0.2, 0.3, 0.5)$, inertia coefficient $(F_s = 0.7, 0.9, 1.1, 1.3)$, thermal radiation $(R = 0.2, 0.3, 0.4, 0.5)$, $(\varepsilon = 0.2, 0.3, 0.4, 0.5)$, fluid parameter $(\in = 3, 3.4, 3.8, 4.2)$, Eckert number $(Ec = 0.002, 0.003, 0.004, 0.005)$, heat source $(Q = 0.02, 0.03, 0.04, 0.05)$, thermal relaxation parameter $(\beta_e = 0.02, 0.03, 0.04, 0.05)$, and latent heat of the fluid parameter $(\lambda = 1, 1.4, 1.8, 2.2)$, as shown in Tables 2–5 in the case of melting and non-melting. In addition to the quantitative results, the findings of the artificial neural network model demonstrate a favorable outcome. Thus far, the findings of this investigation have indicated that the ANN has the capability to accurately forecast both skin friction and heat transfer rate.

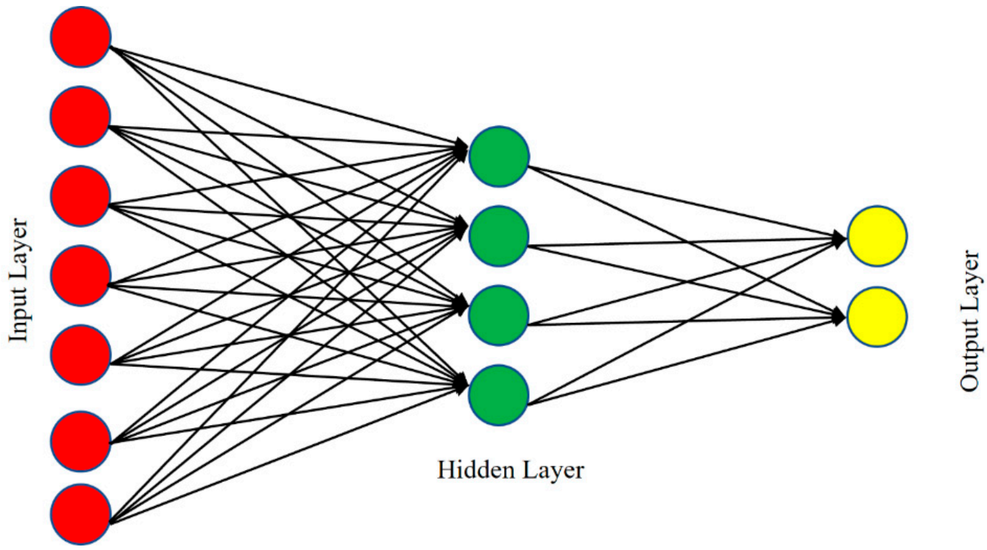

Figure 3. Schematic representation of a multi-layer ANN model.

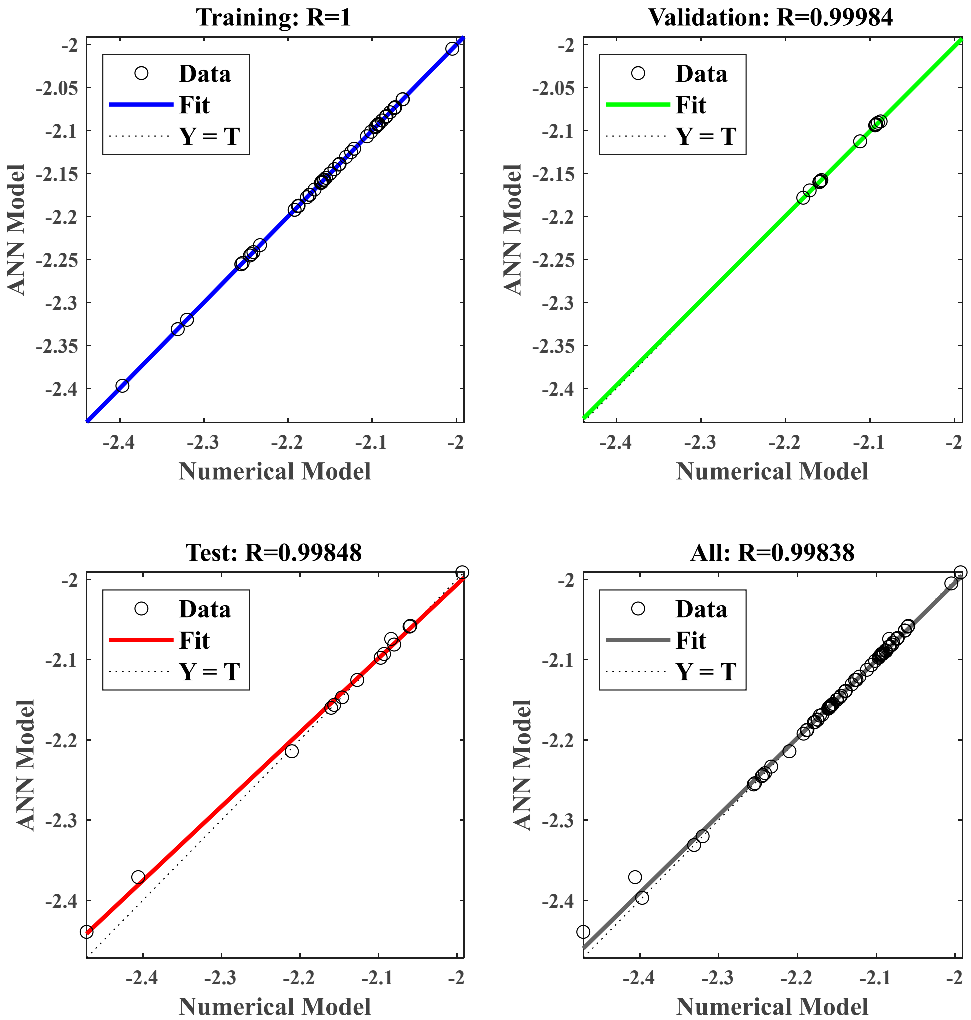

Figure 4. Pictorial illustration of skin friction.

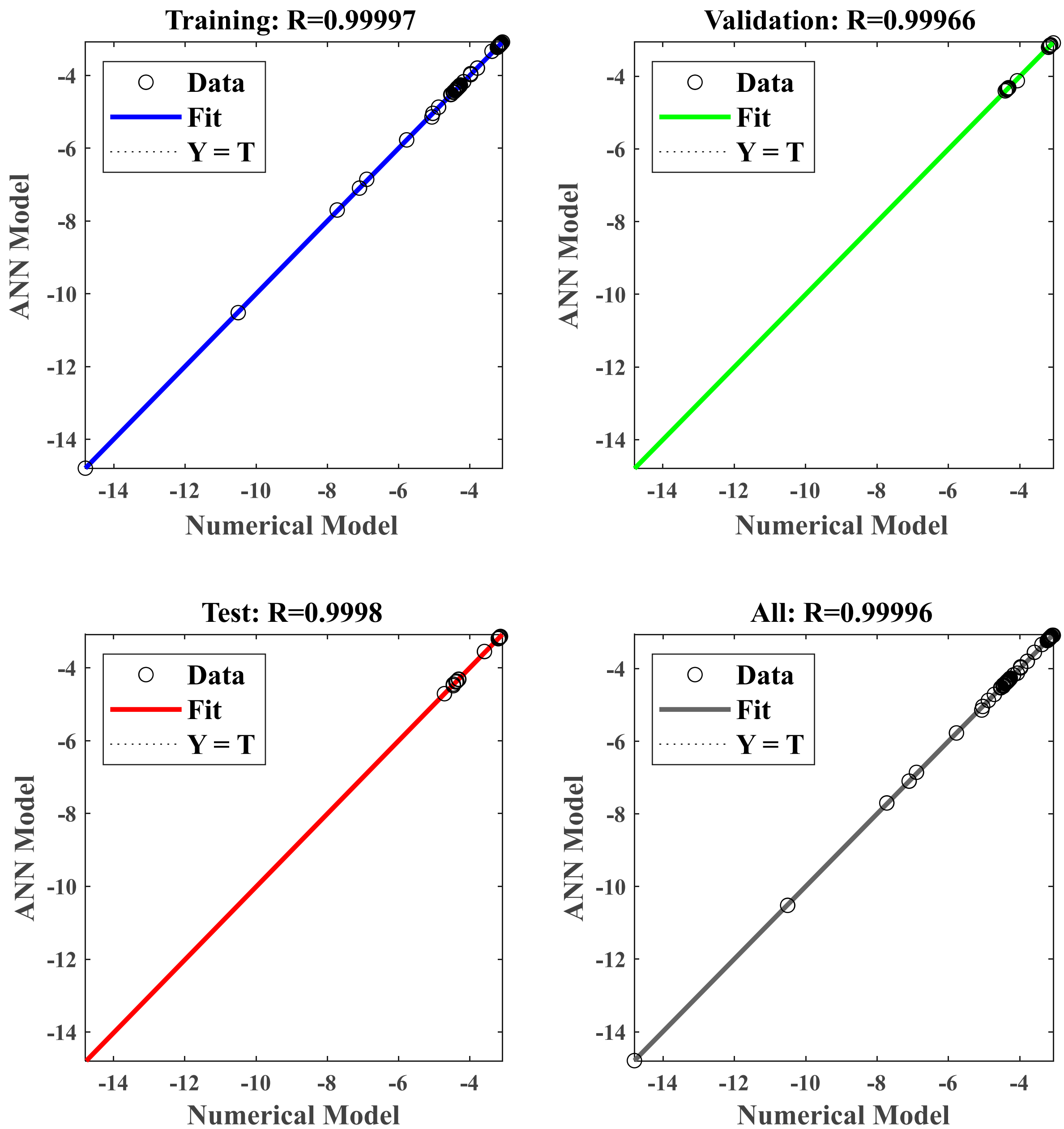

Figure 5. Pictorial illustration of the Nusselt number.

Table 2. Numerical and ANN values of $C_f Re_x^{1/2}/2$ at $Me = 0$.

β_f	K	α	δ	F_s	ε	$\in$	Ec	R	Q	β_e	λ	Me = 0, $C_f Re_x^{1/2}/2$		Error
												NM	ANN	
1	1	2	0.1	1	0.1	4	0.001	0.1	0.01	0.01	2	−2.14629	−2.14693	6.39×10^{-4}
1.5	1	2	0.1	1	0.1	4	0.001	0.1	0.01	0.01	2	−2.15761	−2.15757	3.89×10^{-5}
2	1	2	0.1	1	0.1	4	0.001	0.1	0.01	0.01	2	−2.16858	−2.16858	3.46×10^{-6}

Table 2. *Cont.*

β_f	K	α	δ	F_s	ε	$\in$	Ec	R	Q	β_e	λ	$Me = 0$, $C_f Re_x^{1/2}/2$		Error
												NM	ANN	
2.5	1	2	0.1	1	0.1	4	0.001	0.1	0.01	0.01	2	−2.17920	−2.17813	1.08×10^{-3}
1.6	0.7	2	0.1	1	0.1	4	0.001	0.1	0.01	0.01	2	−2.05934	−2.05772	1.61×10^{-3}
1.6	0.9	2	0.1	1	0.1	4	0.001	0.1	0.01	0.01	2	−2.12691	−2.12527	1.63×10^{-3}
1.6	1.1	2	0.1	1	0.1	4	0.001	0.1	0.01	0.01	2	−2.19223	−2.19220	2.70×10^{-5}
1.6	1.3	2	0.1	1	0.1	4	0.001	0.1	0.01	0.01	2	−2.25552	−2.25553	1.71×10^{-6}
1.6	1	1.4	0.1	1	0.1	4	0.001	0.1	0.01	0.01	2	−2.23333	−2.23325	8.69×10^{-5}
1.6	1	1.8	0.1	1	0.1	4	0.001	0.1	0.01	0.01	2	−2.17433	−2.17491	5.85×10^{-4}
1.6	1	2.2	0.1	1	0.1	4	0.001	0.1	0.01	0.01	2	−2.15013	−2.15015	1.76×10^{-5}
1.6	1	2.6	0.1	1	0.1	4	0.001	0.1	0.01	0.01	2	−2.13867	−2.13875	8.61×10^{-5}
1.6	1	2	0.2	1	0.1	4	0.001	0.1	0.01	0.01	2	−2.15493	−2.15498	5.05×10^{-5}
1.6	1	2	0.3	1	0.1	4	0.001	0.1	0.01	0.01	2	−2.14993	−2.15001	8.15×10^{-5}
1.6	1	2	0.4	1	0.1	4	0.001	0.1	0.01	0.01	2	−2.14482	−2.14486	4.30×10^{-5}
1.6	1	2	0.5	1	0.1	4	0.001	0.1	0.01	0.01	2	−2.13959	−2.13953	6.29×10^{-5}
1.6	1	2	0.1	0.7	0.1	4	0.001	0.1	0.01	0.01	2	−2.07261	−2.07273	1.18×10^{-4}
1.6	1	2	0.1	0.9	0.1	4	0.001	0.1	0.01	0.01	2	−2.13114	−2.13070	4.47×10^{-4}
1.6	1	2	0.1	1.1	0.1	4	0.001	0.1	0.01	0.01	2	−2.18816	−2.18772	4.39×10^{-4}
1.6	1	2	0.1	1.3	0.1	4	0.001	0.1	0.01	0.01	2	−2.24376	−2.24381	4.89×10^{-5}
1.6	1	2	0.1	1	0.2	4	0.001	0.1	0.01	0.01	2	−2.24119	−2.24138	1.87×10^{-4}
1.6	1	2	0.1	1	0.3	4	0.001	0.1	0.01	0.01	2	−2.32018	−2.32011	6.60×10^{-5}
1.6	1	2	0.1	1	0.4	4	0.001	0.1	0.01	0.01	2	−2.39694	−2.39694	5.52×10^{-6}
1.6	1	2	0.1	1	0.5	4	0.001	0.1	0.01	0.01	2	−2.47161	−2.43942	3.22×10^{-2}
1.6	1	2	0.1	1	0.1	3	0.001	0.1	0.01	0.01	2	−2.16066	−2.16068	2.24×10^{-5}
1.6	1	2	0.1	1	0.1	3.4	0.001	0.1	0.01	0.01	2	−2.16033	−2.16027	5.63×10^{-5}
1.6	1	2	0.1	1	0.1	3.8	0.001	0.1	0.01	0.01	2	−2.16000	−2.15992	7.61×10^{-5}
1.6	1	2	0.1	1	0.1	4.2	0.001	0.1	0.01	0.01	2	−2.15967	−2.15964	2.82×10^{-5}
1.6	1	2	0.1	1	0.1	4	0.002	0.1	0.01	0.01	2	−2.15987	−2.15984	3.37×10^{-5}
1.6	1	2	0.1	1	0.1	4	0.003	0.1	0.01	0.01	2	−2.15991	−2.15994	2.05×10^{-5}
1.6	1	2	0.1	1	0.1	4	0.004	0.1	0.01	0.01	2	−2.15996	−2.16000	4.62×10^{-5}
1.6	1	2	0.1	1	0.1	4	0.005	0.1	0.01	0.01	2	−2.16000	−2.15996	3.73×10^{-5}
1.6	1	2	0.1	1	0.1	4	0.001	0.2	0.01	0.01	2	−2.15882	−2.15878	3.65×10^{-5}
1.6	1	2	0.1	1	0.1	4	0.001	0.3	0.01	0.01	2	−2.15788	−2.15786	1.57×10^{-5}
1.6	1	2	0.1	1	0.1	4	0.001	0.4	0.01	0.01	2	−2.15701	−2.15703	1.61×10^{-5}
1.6	1	2	0.1	1	0.1	4	0.001	0.5	0.01	0.01	2	−2.15621	−2.15628	7.14×10^{-5}
1.6	1	2	0.1	1	0.1	4	0.001	0.1	0.02	0.01	2	−2.17153	−2.16959	1.95×10^{-3}

Table 2. *Cont.*

β_f	K	α	δ	F_s	ε	$\in$	Ec	R	Q	β_e	λ	$Me = 0$, $C_f Re_x^{1/2}/2$		Error
												NM	ANN	
1.6	1	2	0.1	1	0.1	4	0.001	0.1	0.03	0.01	2	−2.18749	−2.18737	1.22×10^{-4}
1.6	1	2	0.1	1	0.1	4	0.001	0.1	0.04	0.01	2	−2.21017	−2.21418	4.01×10^{-3}
1.6	1	2	0.1	1	0.1	4	0.001	0.1	0.05	0.01	2	−2.24532	−2.24534	1.76×10^{-5}
1.6	1	2	0.1	1	0.1	4	0.001	0.1	0.01	0.02	2	−2.15978	−2.15978	3.12×10^{-6}
1.6	1	2	0.1	1	0.1	4	0.001	0.1	0.01	0.03	2	−2.15973	−2.15978	5.15×10^{-5}
1.6	1	2	0.1	1	0.1	4	0.001	0.1	0.01	0.04	2	−2.15968	−2.15974	5.59×10^{-5}
1.6	1	2	0.1	1	0.1	4	0.001	0.1	0.01	0.05	2	−2.15963	−2.15958	5.49×10^{-5}
1.6	1	2	0.1	1	0.1	4	0.001	0.1	0.01	0.01	1	−2.16100	−2.16100	9.01×10^{-6}
1.6	1	2	0.1	1	0.1	4	0.001	0.1	0.01	0.01	1.4	−2.16054	−2.16054	6.13×10^{-6}
1.6	1	2	0.1	1	0.1	4	0.001	0.1	0.01	0.01	1.8	−2.16007	−2.16002	5.04×10^{-5}
1.6	1	2	0.1	1	0.1	4	0.001	0.1	0.01	0.01	2.2	−2.15960	−2.15955	4.52×10^{-5}

Mean square error: 0.0000248262.

Table 3. Numerical and ANN values of $C_f Re_x^{1/2}/2$ at $Me = 1$.

β_f	K	α	δ	F_s	ε	$\in$	Ec	R	Q	β_e	λ	$Me = 1$, $C_f Re_x^{1/2}/2$		Error
												NM	ANN	
1	1	2	0.1	1	0.1	4	0.001	0.1	0.01	0.01	2	−2.07988	−2.08102	1.14×10^{-3}
1.5	1	2	0.1	1	0.1	4	0.001	0.1	0.01	0.01	2	−2.09074	−2.09097	2.28×10^{-4}
2	1	2	0.1	1	0.1	4	0.001	0.1	0.01	0.01	2	−2.10138	−2.10139	4.32×10^{-6}
2.5	1	2	0.1	1	0.1	4	0.001	0.1	0.01	0.01	2	−2.11181	−2.11256	7.49×10^{-4}
1.6	0.7	2	0.1	1	0.1	4	0.001	0.1	0.01	0.01	2	−1.99306	−1.99095	2.12×10^{-3}
1.6	0.9	2	0.1	1	0.1	4	0.001	0.1	0.01	0.01	2	−2.06017	−2.05865	1.52×10^{-3}
1.6	1.1	2	0.1	1	0.1	4	0.001	0.1	0.01	0.01	2	−2.12507	−2.12511	3.84×10^{-5}
1.6	1.3	2	0.1	1	0.1	4	0.001	0.1	0.01	0.01	2	−2.18797	−2.18796	6.75×10^{-6}
1.6	1	1.4	0.1	1	0.1	4	0.001	0.1	0.01	0.01	2	−2.16018	−2.16012	5.66×10^{-5}
1.6	1	1.8	0.1	1	0.1	4	0.001	0.1	0.01	0.01	2	−2.10618	−2.10667	4.87×10^{-4}
1.6	1	2.2	0.1	1	0.1	4	0.001	0.1	0.01	0.01	2	−2.08394	−2.08420	2.59×10^{-4}
1.6	1	2.6	0.1	1	0.1	4	0.001	0.1	0.01	0.01	2	−2.07330	−2.07332	2.71×10^{-5}
1.6	1	2	0.2	1	0.1	4	0.001	0.1	0.01	0.01	2	−2.08825	−2.08824	1.33×10^{-5}
1.6	1	2	0.3	1	0.1	4	0.001	0.1	0.01	0.01	2	−2.08354	−2.08343	1.08×10^{-4}
1.6	1	2	0.4	1	0.1	4	0.001	0.1	0.01	0.01	2	−2.07873	−2.07864	9.23×10^{-5}
1.6	1	2	0.5	1	0.1	4	0.001	0.1	0.01	0.01	2	−2.07382	−2.07394	1.14×10^{-4}
1.6	1	2	0.1	0.7	0.1	4	0.001	0.1	0.01	0.01	2	−2.00482	−2.00479	2.88×10^{-5}
1.6	1	2	0.1	0.9	0.1	4	0.001	0.1	0.01	0.01	2	−2.06393	−2.06365	2.79×10^{-4}

Table 3. *Cont.*

β_f	K	α	δ	F_s	ε	$\in$	Ec	R	Q	β_e	λ	$Me = 1$, $C_f Re_x^{1/2}/2$		Error
												NM	ANN	
1.6	1	2	0.1	1.1	0.1	4	0.001	0.1	0.01	0.01	2	−2.12146	−2.12110	3.60×10^{-4}
1.6	1	2	0.1	1.3	0.1	4	0.001	0.1	0.01	0.01	2	−2.17754	−2.17758	3.53×10^{-5}
1.6	1	2	0.1	1	0.2	4	0.001	0.1	0.01	0.01	2	−2.17467	−2.17453	1.42×10^{-4}
1.6	1	2	0.1	1	0.3	4	0.001	0.1	0.01	0.01	2	−2.25400	−2.25404	4.17×10^{-5}
1.6	1	2	0.1	1	0.4	4	0.001	0.1	0.01	0.01	2	−2.33104	−2.33104	1.07×10^{-7}
1.6	1	2	0.1	1	0.5	4	0.001	0.1	0.01	0.01	2	−2.40594	−2.37111	3.48×10^{-2}
1.6	1	2	0.1	1	0.1	3	0.001	0.1	0.01	0.01	2	−2.09243	−2.09248	4.99×10^{-5}
1.6	1	2	0.1	1	0.1	3.4	0.001	0.1	0.01	0.01	2	−2.09261	−2.09254	6.80×10^{-5}
1.6	1	2	0.1	1	0.1	3.8	0.001	0.1	0.01	0.01	2	−2.09279	−2.09280	4.96×10^{-6}
1.6	1	2	0.1	1	0.1	4.2	0.001	0.1	0.01	0.01	2	−2.09298	−2.09327	2.95×10^{-4}
1.6	1	2	0.1	1	0.1	4	0.002	0.1	0.01	0.01	2	−2.09273	−2.09271	1.44×10^{-5}
1.6	1	2	0.1	1	0.1	4	0.003	0.1	0.01	0.01	2	−2.09257	−2.09249	7.43×10^{-5}
1.6	1	2	0.1	1	0.1	4	0.004	0.1	0.01	0.01	2	−2.09241	−2.09236	4.96×10^{-5}
1.6	1	2	0.1	1	0.1	4	0.005	0.1	0.01	0.01	2	−2.09225	−2.09232	7.08×10^{-5}
1.6	1	2	0.1	1	0.1	4	0.001	0.2	0.01	0.01	2	−2.09400	−2.09391	9.21×10^{-5}
1.6	1	2	0.1	1	0.1	4	0.001	0.3	0.01	0.01	2	−2.09506	−2.09495	1.13×10^{-4}
1.6	1	2	0.1	1	0.1	4	0.001	0.4	0.01	0.01	2	−2.09607	−2.09614	7.37×10^{-5}
1.6	1	2	0.1	1	0.1	4	0.001	0.5	0.01	0.01	2	−2.09701	−2.09749	4.84×10^{-4}
1.6	1	2	0.1	1	0.1	4	0.001	0.1	0.02	0.01	2	−2.08759	−2.08934	1.76×10^{-3}
1.6	1	2	0.1	1	0.1	4	0.001	0.1	0.03	0.01	2	−2.08300	−2.08313	1.34×10^{-4}
1.6	1	2	0.1	1	0.1	4	0.001	0.1	0.04	0.01	2	−2.08369	−2.07403	9.66×10^{-3}
1.6	1	2	0.1	1	0.1	4	0.001	0.1	0.05	0.01	2	−2.06357	−2.06354	2.55×10^{-5}
1.6	1	2	0.1	1	0.1	4	0.001	0.1	0.01	0.02	2	−2.09293	−2.09290	2.99×10^{-5}
1.6	1	2	0.1	1	0.1	4	0.001	0.1	0.01	0.03	2	−2.09297	−2.09288	9.26×10^{-5}
1.6	1	2	0.1	1	0.1	4	0.001	0.1	0.01	0.04	2	−2.09301	−2.09296	5.65×10^{-5}
1.6	1	2	0.1	1	0.1	4	0.001	0.1	0.01	0.05	2	−2.09306	−2.09315	8.98×10^{-5}
1.6	1	2	0.1	1	0.1	4	0.001	0.1	0.01	0.01	1	−2.09226	−2.09227	1.30×10^{-5}
1.6	1	2	0.1	1	0.1	4	0.001	0.1	0.01	0.01	1.4	−2.09250	−2.09254	3.04×10^{-5}
1.6	1	2	0.1	1	0.1	4	0.001	0.1	0.01	0.01	1.8	−2.09276	−2.09284	8.32×10^{-5}
1.6	1	2	0.1	1	0.1	4	0.001	0.1	0.01	0.01	2.2	−2.09301	−2.09318	1.67×10^{-4}

Mean square error: 0.0000248262.

Table 4. Numerical and ANN values of $\mathrm{Nu}_x Re_x^{-1/2}$ at $Me = 0$.

β_f	K	α	δ	F_s	ε	$\in$	Ec	R	Q	β_e	λ	$Me = 0$, $\mathrm{Nu}_x Re_x^{-1/2}$ NM	ANN	Error
1	1	2	0.1	1	0.1	4	0.001	0.1	0.01	0.01	2	−4.46089	−4.44791	1.30×10^{-2}
1.5	1	2	0.1	1	0.1	4	0.001	0.1	0.01	0.01	2	−4.36548	−4.36510	3.80×10^{-4}
2	1	2	0.1	1	0.1	4	0.001	0.1	0.01	0.01	2	−4.27002	−4.27390	3.88×10^{-3}
2.5	1	2	0.1	1	0.1	4	0.001	0.1	0.01	0.01	2	−4.17453	−4.17302	1.51×10^{-3}
1.6	0.7	2	0.1	1	0.1	4	0.001	0.1	0.01	0.01	2	−4.31002	−4.31532	5.30×10^{-3}
1.6	0.9	2	0.1	1	0.1	4	0.001	0.1	0.01	0.01	2	−4.33456	−4.33673	2.17×10^{-3}
1.6	1.1	2	0.1	1	0.1	4	0.001	0.1	0.01	0.01	2	−4.35796	−4.35851	5.53×10^{-4}
1.6	1.3	2	0.1	1	0.1	4	0.001	0.1	0.01	0.01	2	−4.38036	−4.38067	3.10×10^{-4}
1.6	1	1.4	0.1	1	0.1	4	0.001	0.1	0.01	0.01	2	−4.06652	−4.12323	5.67×10^{-2}
1.6	1	1.8	0.1	1	0.1	4	0.001	0.1	0.01	0.01	2	−4.28092	−4.28388	2.97×10^{-3}
1.6	1	2.2	0.1	1	0.1	4	0.001	0.1	0.01	0.01	2	−4.39588	−4.40198	6.10×10^{-3}
1.6	1	2.6	0.1	1	0.1	4	0.001	0.1	0.01	0.01	2	−4.46448	−4.48764	2.32×10^{-2}
1.6	1	2	0.2	1	0.1	4	0.001	0.1	0.01	0.01	2	−4.34602	−4.34650	4.72×10^{-4}
1.6	1	2	0.3	1	0.1	4	0.001	0.1	0.01	0.01	2	−4.34563	−4.34545	1.80×10^{-4}
1.6	1	2	0.4	1	0.1	4	0.001	0.1	0.01	0.01	2	−4.34520	−4.34445	7.53×10^{-4}
1.6	1	2	0.5	1	0.1	4	0.001	0.1	0.01	0.01	2	−4.34474	−4.34353	1.21×10^{-3}
1.6	1	2	0.1	0.7	0.1	4	0.001	0.1	0.01	0.01	2	−4.34153	−4.34260	1.07×10^{-3}
1.6	1	2	0.1	0.9	0.1	4	0.001	0.1	0.01	0.01	2	−4.34477	−4.34593	1.16×10^{-3}
1.6	1	2	0.1	1.1	0.1	4	0.001	0.1	0.01	0.01	2	−4.34801	−4.34920	1.19×10^{-3}
1.6	1	2	0.1	1.3	0.1	4	0.001	0.1	0.01	0.01	2	−4.35124	−4.35240	1.16×10^{-3}
1.6	1	2	0.1	1	0.2	4	0.001	0.1	0.01	0.01	2	−4.32180	−4.32562	3.82×10^{-3}
1.6	1	2	0.1	1	0.3	4	0.001	0.1	0.01	0.01	2	−4.30032	−4.30375	3.43×10^{-3}
1.6	1	2	0.1	1	0.4	4	0.001	0.1	0.01	0.01	2	−4.28137	−4.28204	6.70×10^{-4}
1.6	1	2	0.1	1	0.5	4	0.001	0.1	0.01	0.01	2	−4.26451	−4.26063	3.88×10^{-3}
1.6	1	2	0.1	1	0.1	3	0.001	0.1	0.01	0.01	2	−4.46625	−4.46469	1.56×10^{-3}
1.6	1	2	0.1	1	0.1	3.4	0.001	0.1	0.01	0.01	2	−4.41831	−4.41871	4.10×10^{-4}
1.6	1	2	0.1	1	0.1	3.8	0.001	0.1	0.01	0.01	2	−4.37036	−4.37163	1.27×10^{-3}
1.6	1	2	0.1	1	0.1	4.2	0.001	0.1	0.01	0.01	2	−4.32242	−4.32313	7.07×10^{-4}
1.6	1	2	0.1	1	0.1	4	0.002	0.1	0.01	0.01	2	−4.36086	−4.36031	5.53×10^{-4}
1.6	1	2	0.1	1	0.1	4	0.003	0.1	0.01	0.01	2	−4.37533	−4.37336	1.97×10^{-3}
1.6	1	2	0.1	1	0.1	4	0.004	0.1	0.01	0.01	2	−4.38980	−4.38699	2.81×10^{-3}
1.6	1	2	0.1	1	0.1	4	0.005	0.1	0.01	0.01	2	−4.40427	−4.40186	2.41×10^{-3}
1.6	1	2	0.1	1	0.1	4	0.001	0.2	0.01	0.01	2	−4.53531	−4.52760	7.71×10^{-3}
1.6	1	2	0.1	1	0.1	4	0.001	0.3	0.01	0.01	2	−4.71261	−4.70877	3.84×10^{-3}

Table 4. *Cont.*

β_f	K	α	δ	F_s	ε	$\in$	Ec	R	Q	β_e	λ	Me = 0, $Nu_x Re_x^{-1/2}$ NM	ANN	Error
1.6	1	2	0.1	1	0.1	4	0.001	0.4	0.01	0.01	2	−4.87976	−4.87325	6.51×10^{-3}
1.6	1	2	0.1	1	0.1	4	0.001	0.5	0.01	0.01	2	−5.03796	−5.04091	2.94×10^{-3}
1.6	1	2	0.1	1	0.1	4	0.001	0.1	0.02	0.01	2	−5.77414	−5.77091	3.23×10^{-3}
1.6	1	2	0.1	1	0.1	4	0.001	0.1	0.03	0.01	2	−7.72720	−7.69848	2.87×10^{-2}
1.6	1	2	0.1	1	0.1	4	0.001	0.1	0.04	0.01	2	−10.50691	−10.51817	1.13×10^{-2}
1.6	1	2	0.1	1	0.1	4	0.001	0.1	0.05	0.01	2	−14.80148	−14.79289	8.59×10^{-3}
1.6	1	2	0.1	1	0.1	4	0.001	0.1	0.01	0.02	2	−4.33180	−4.33348	1.68×10^{-3}
1.6	1	2	0.1	1	0.1	4	0.001	0.1	0.01	0.03	2	−4.31720	−4.31861	1.42×10^{-3}
1.6	1	2	0.1	1	0.1	4	0.001	0.1	0.01	0.04	2	−4.30259	−4.30294	3.50×10^{-4}
1.6	1	2	0.1	1	0.1	4	0.001	0.1	0.01	0.05	2	−4.28796	−4.28642	1.55×10^{-3}
1.6	1	2	0.1	1	0.1	4	0.001	0.1	0.01	0.01	1	−4.51998	−4.51681	3.16×10^{-3}
1.6	1	2	0.1	1	0.1	4	0.001	0.1	0.01	0.01	1.4	−4.45083	−4.45203	1.19×10^{-3}
1.6	1	2	0.1	1	0.1	4	0.001	0.1	0.01	0.01	1.8	−4.38130	−4.38344	2.14×10^{-3}
1.6	1	2	0.1	1	0.1	4	0.001	0.1	0.01	0.01	2.2	−4.31138	−4.31057	8.12×10^{-4}

Mean square error: 0.000184568.

Table 5. Numerical and ANN values of $Nu_x Re_x^{-1/2}$ at $Me = 1$.

β_f	K	α	δ	F_s	ε	$\in$	Ec	R	Q	β_e	λ	Me = 1, $Nu_x Re_x^{-1/2}$ NM	ANN	Error
1	1	2	0.1	1	0.1	4	0.001	0.1	0.01	0.01	2	−3.20072	−3.19661	1.30×10^{-2}
1.5	1	2	0.1	1	0.1	4	0.001	0.1	0.01	0.01	2	−3.16211	−3.16133	3.80×10^{-4}
2	1	2	0.1	1	0.1	4	0.001	0.1	0.01	0.01	2	−3.12310	−3.12346	3.88×10^{-3}
2.5	1	2	0.1	1	0.1	4	0.001	0.1	0.01	0.01	2	−3.08368	−3.08257	1.51×10^{-3}
1.6	0.7	2	0.1	1	0.1	4	0.001	0.1	0.01	0.01	2	−3.13264	−3.13369	5.30×10^{-3}
1.6	0.9	2	0.1	1	0.1	4	0.001	0.1	0.01	0.01	2	−3.14724	−3.14715	2.17×10^{-3}
1.6	1.1	2	0.1	1	0.1	4	0.001	0.1	0.01	0.01	2	−3.16133	−3.16087	5.53×10^{-4}
1.6	1.3	2	0.1	1	0.1	4	0.001	0.1	0.01	0.01	2	−3.17500	−3.17482	3.10×10^{-4}
1.6	1	1.4	0.1	1	0.1	4	0.001	0.1	0.01	0.01	2	−3.05836	−3.08342	5.67×10^{-2}
1.6	1	1.8	0.1	1	0.1	4	0.001	0.1	0.01	0.01	2	−3.13077	−3.13409	2.97×10^{-3}
1.6	1	2.2	0.1	1	0.1	4	0.001	0.1	0.01	0.01	2	−3.17264	−3.17082	6.10×10^{-3}
1.6	1	2.6	0.1	1	0.1	4	0.001	0.1	0.01	0.01	2	−3.19874	−3.19692	2.32×10^{-2}
1.6	1	2	0.2	1	0.1	4	0.001	0.1	0.01	0.01	2	−3.15385	−3.15368	4.72×10^{-4}

Table 5. *Cont.*

β_f	K	α	δ	F_s	ε	$\in$	Ec	R	Q	β_e	λ	$Me = 1$, $Nu_x Re_x^{-1/2}$ NM	ANN	Error
1.6	1	2	0.3	1	0.1	4	0.001	0.1	0.01	0.01	2	−3.15333	−3.15341	1.80×10^{-4}
1.6	1	2	0.4	1	0.1	4	0.001	0.1	0.01	0.01	2	−3.15279	−3.15321	7.53×10^{-4}
1.6	1	2	0.5	1	0.1	4	0.001	0.1	0.01	0.01	2	−3.15222	−3.15313	1.21×10^{-3}
1.6	1	2	0.1	0.7	0.1	4	0.001	0.1	0.01	0.01	2	−3.15358	−3.15319	1.07×10^{-3}
1.6	1	2	0.1	0.9	0.1	4	0.001	0.1	0.01	0.01	2	−3.15407	−3.15372	1.16×10^{-3}
1.6	1	2	0.1	1.1	0.1	4	0.001	0.1	0.01	0.01	2	−3.15463	−3.15423	1.19×10^{-3}
1.6	1	2	0.1	1.3	0.1	4	0.001	0.1	0.01	0.01	2	−3.15525	−3.15472	1.16×10^{-3}
1.6	1	2	0.1	1	0.2	4	0.001	0.1	0.01	0.01	2	−3.14099	−3.14250	3.82×10^{-3}
1.6	1	2	0.1	1	0.3	4	0.001	0.1	0.01	0.01	2	−3.12958	−3.13117	3.43×10^{-3}
1.6	1	2	0.1	1	0.4	4	0.001	0.1	0.01	0.01	2	−3.11970	−3.12007	6.70×10^{-4}
1.6	1	2	0.1	1	0.5	4	0.001	0.1	0.01	0.01	2	−3.11107	−3.10940	3.88×10^{-3}
1.6	1	2	0.1	1	0.1	3	0.001	0.1	0.01	0.01	2	−3.20773	−3.20859	1.56×10^{-3}
1.6	1	2	0.1	1	0.1	3.4	0.001	0.1	0.01	0.01	2	−3.18650	−3.18675	4.10×10^{-4}
1.6	1	2	0.1	1	0.1	3.8	0.001	0.1	0.01	0.01	2	−3.16511	−3.16496	1.27×10^{-3}
1.6	1	2	0.1	1	0.1	4.2	0.001	0.1	0.01	0.01	2	−3.14354	−3.14291	7.07×10^{-4}
1.6	1	2	0.1	1	0.1	4	0.002	0.1	0.01	0.01	2	−3.16387	−3.16478	5.53×10^{-4}
1.6	1	2	0.1	1	0.1	4	0.003	0.1	0.01	0.01	2	−3.17339	−3.17595	1.97×10^{-3}
1.6	1	2	0.1	1	0.1	4	0.004	0.1	0.01	0.01	2	−3.18290	−3.18785	2.81×10^{-3}
1.6	1	2	0.1	1	0.1	4	0.005	0.1	0.01	0.01	2	−3.19241	−3.20137	2.41×10^{-3}
1.6	1	2	0.1	1	0.1	4	0.001	0.2	0.01	0.01	2	−3.37827	−3.33465	7.71×10^{-3}
1.6	1	2	0.1	1	0.1	4	0.001	0.3	0.01	0.01	2	−3.58902	−3.55032	3.84×10^{-3}
1.6	1	2	0.1	1	0.1	4	0.001	0.4	0.01	0.01	2	−3.78802	−3.79790	6.51×10^{-3}
1.6	1	2	0.1	1	0.1	4	0.001	0.5	0.01	0.01	2	−3.97645	−3.97821	2.94×10^{-3}
1.6	1	2	0.1	1	0.1	4	0.001	0.1	0.02	0.01	2	−3.97780	−3.95129	3.23×10^{-3}
1.6	1	2	0.1	1	0.1	4	0.001	0.1	0.03	0.01	2	−5.06543	−5.14094	2.87×10^{-2}
1.6	1	2	0.1	1	0.1	4	0.001	0.1	0.04	0.01	2	−6.89639	−6.85484	1.13×10^{-2}
1.6	1	2	0.1	1	0.1	4	0.001	0.1	0.05	0.01	2	−7.10072	−7.09668	8.59×10^{-3}
1.6	1	2	0.1	1	0.1	4	0.001	0.1	0.01	0.02	2	−3.15050	−3.15059	1.68×10^{-3}
1.6	1	2	0.1	1	0.1	4	0.001	0.1	0.01	0.03	2	−3.14662	−3.14695	1.42×10^{-3}
1.6	1	2	0.1	1	0.1	4	0.001	0.1	0.01	0.04	2	−3.14272	−3.14305	3.50×10^{-4}
1.6	1	2	0.1	1	0.1	4	0.001	0.1	0.01	0.05	2	−3.13878	−3.13888	1.55×10^{-3}
1.6	1	2	0.1	1	0.1	4	0.001	0.1	0.01	0.01	1	−3.22881	−3.23008	3.16×10^{-3}
1.6	1	2	0.1	1	0.1	4	0.001	0.1	0.01	0.01	1.4	−3.19942	−3.20047	1.19×10^{-3}
1.6	1	2	0.1	1	0.1	4	0.001	0.1	0.01	0.01	1.8	−3.16950	−3.16978	2.14×10^{-3}
1.6	1	2	0.1	1	0.1	4	0.001	0.1	0.01	0.01	2.2	−3.13905	−3.13785	8.12×10^{-4}

Mean square error: 0.000184568.

6. Results and Discussion

The objective of this section is to illustrate the impact of entropy production and melting heat transfer on the ferrohydrodynamic flow of a hybrid nanofluid consisting of iron oxide (Fe_3O_4) and gold (Au) particles suspended in blood, utilizing a non-Fourier heat flux model based on the Powell–Eyring equation. This section discusses the significance of momentum and thermal properties in relation to important parameters, including the ferromagnetic parameter $\left(\beta_f = 0.0, 1.0, 3.0, 5.0\right)$, fluid parameter $(\in = 0.0, 1.0, 3.0, 5.0)$, inertia coefficient $(F_s = 0.0, 1.0, 3.0, 5.0)$, porosity parameter $(K = 0.0, 1.0, 3.0, 5.0)$, heat source $(Q = -0.01, -0.005, 0.00, 0.01)$, nanoparticle volume fraction $(\phi = 0.00, 0.01, 0.03, 0.05)$, latent heat of the fluid parameter $(\lambda = 1.0, 3.0, 5.0, 7.0)$, Eckert number $(E_c = 0.0, 0.1, 0.2, 0.3)$, thermal relaxation parameter $(\beta_e = 0.0, 0.2, 0.4, 0.6)$, and radiation $(R = 0.0, 1.0, 2.0, 3.0)$; the Fe_3O_4-Au/blood hybrid nanofluid velocity $(f'(\eta))$, temperature $(\theta_1(\eta))$, entropy generation, skin friction $C_f Re_x^{1/2}/2$, and Nusselt number $-Nu_x Re_x^{-1/2} x^{-1}$ are visualized and intricately deliberated. The dimensional version of the flow and transport equations is solved using the bvp4c MATLAB program under specific boundary conditions. Solid and dotted lines represent the properties of melting and non-melting heat transmission over the sheet throughout the study. In order to establish the soundness and precision of the suggested methodology, a comparative analysis is conducted between the numerical computations at specific stages and the previous findings of Ishak et al. [24] and Pal [25], and the results of this comparison are presented in Table 6.

Table 6. Comparison of $-\theta\prime(0)$ for several values of Pr with earlier work [24,25], $R = 0$, $\beta_f = 0$, $\beta = 0$, $Ec = 0$, $Q = 0$, $K = 0$, $F_s = 0$.

Pr	**0.72**	**1.0**	**3.0**	**7.0**	**10.0**	**100.0**
Ishak et al. [24] (Exact Sol.)	0.808631350	1.0000	1.923682594	3.072250207	3.720673901	12.29408326
Pal [25]	0.80863135	1.0000	1.92368256	3.07225020	3.72067391	12.2940835
Present results	0.808631	1.0000	1.923683	3.072250	3.720674	12.294083

Figures 6–9 manifest the hybrid nanofluid velocity profile $f'(\eta)$ examined for the ferromagnetic parameter $\left(\beta_f\right)$, fluid parameter $(\in)$, inertia coefficient (F_s), and porosity parameter (K) through numerical investigation. Figure 6 demonstrates that improving the ferromagnetic parameter $\left(\beta_f\right)$ tends to decrease the $f'(\eta)$. Physically, different magnetic parameter values lead to Lorentz force deviation, which makes the transport phenomena more resistant. Figure 7 illustrates how the fluid parameter $(\in)$ influence on velocity profile $f'(\eta)$ changes. According to this graph, the velocity is improved by rising values in the fluid parameter. Physically, an increase in the values of the fluid parameters is observed as fluid velocity greatly increases and fluid viscosity significantly decreases. Figure 8 displays how the velocity profile $f'(\eta)$ and inertia coefficient (F_s) are connected. This graph demonstrates that the velocity decreases with increasing amounts of channel inclination. It is observed that when the inertia coefficient increases, the thermal boundary layer thickens and fluid cannot move naturally. In Figure 9, the influence of the porosity parameter (K) on the velocity profile $f'(\eta)$ is portrayed. This graph demonstrates that the velocity profile $f'(\eta)$ decreases with an increase in the porosity parameter (K). Physically, by increasing the porosity, the pore size of the medium is reduced. The slowing of the fluid flow causes a reduction in fluid velocity.

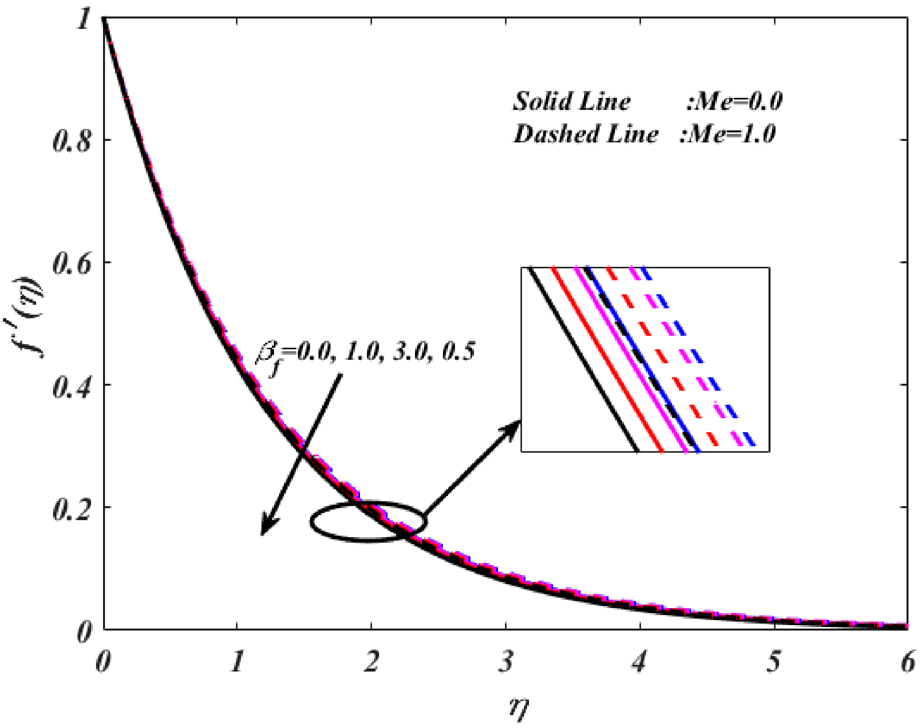

Figure 6. Effects of β_f on $f'(\eta)$.

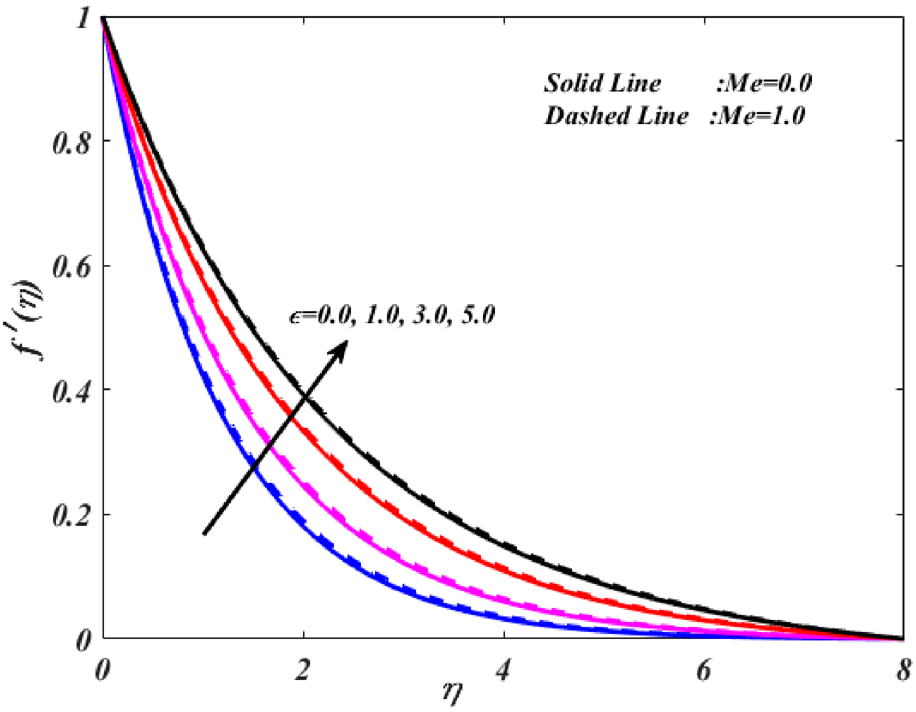

Figure 7. Effects of $\in$ on $f'(\eta)$.

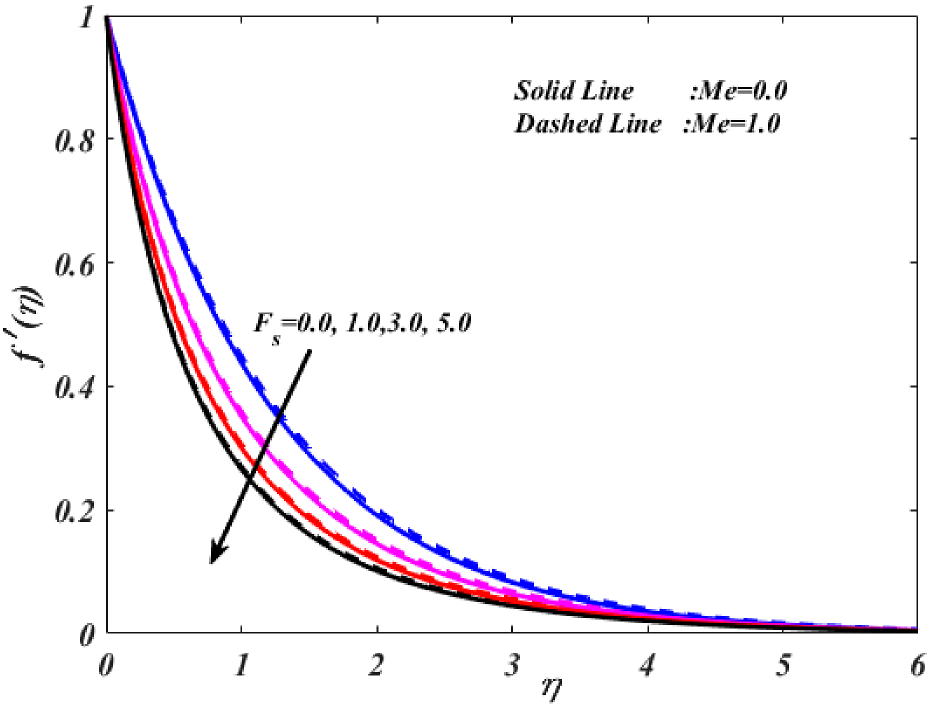

Figure 8. Effects of F_s on $f'(\eta)$.

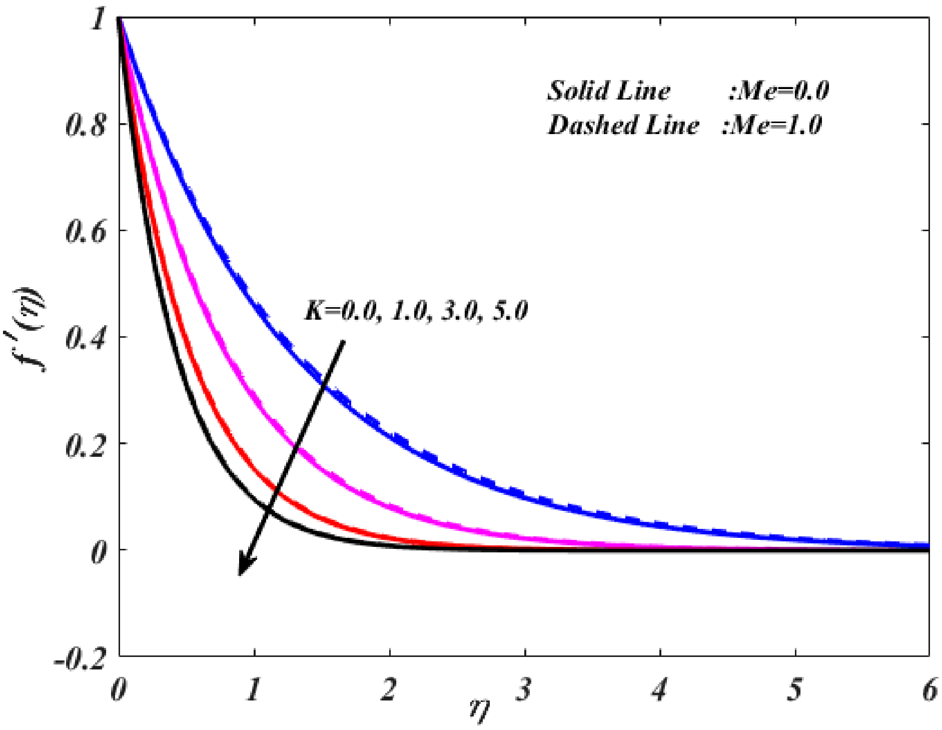

Figure 9. Effects of K on $f'(\eta)$.

Figures 10–16 were plotted to investigate the impact of different active factors on temperature $\theta_1(\eta)$. Figure 10 illustrates the impact of changes in the heat source parameter (Q) on the temperature profile. An increase in the heat source parameter (Q) results in an intensification of the temperature profile, as has been observed. Incorporating external heat into the mechanism results in an increase in the average kinetic energy, leading to a higher rate of particle transfer. Consequently, the temperature of the blood rises. Figure 11 depicts the relationship between the volume fraction (ϕ) of (Fe_3O_4-Au/blood) nanoparticles and temperature $\theta_1(\eta)$. It has been observed that a decrease in temperature $\theta_1(\eta)$ leads to an enhancement in the values of ϕ. Figure 12 depicts the relationship between the latent heat of the fluid parameter (λ) and temperature $\theta_1(\eta)$. It has been identified that increasing temperature can enhance the values of λ. Figure 13 illustrates how the influence of the Eckert number (Ec) on temperature $\theta_1(\eta)$ changes. According to this graph, the temperature is improved by rising values in the (Ec). Physically, a higher (Ec) produces more kinetic energy, causing particles to collide more frequently and dissipate energy. As a result, kinetic energy is converted into thermal energy. Figure 14 explores the effects of the thermal relaxation parameter (β_e) on temperature $\theta_1(\eta)$. It is observed that $\theta_1(\eta)$ declines upon an improvement in (β_e). This is because when the temperature rises, material particles need more time to transfer heat to the particles around them. The temperature profile actually decreases as a result of materials showing a non-conducting behavior at increasing thermal relaxation parameter values. Therefore, it may be inferred that the Cattaneo–Christov heat flux model has fewer temperature profiles than Fourier's law does. The effect of (R) on $\theta_1(\eta)$ is represented in Figure 15. It is detected that an increase in the value of (R) causes $\theta_1(\eta)$ to decline. Increases in (R) values are known to cause a decrease in blood temperature. Due to the boundary conditions, it is ultimately determined that when the fluid is in contact with a higher emissivity, it tends to absorb more radiation and consequently lose more heat to the surroundings. This leads to a decrease in fluid temperature.

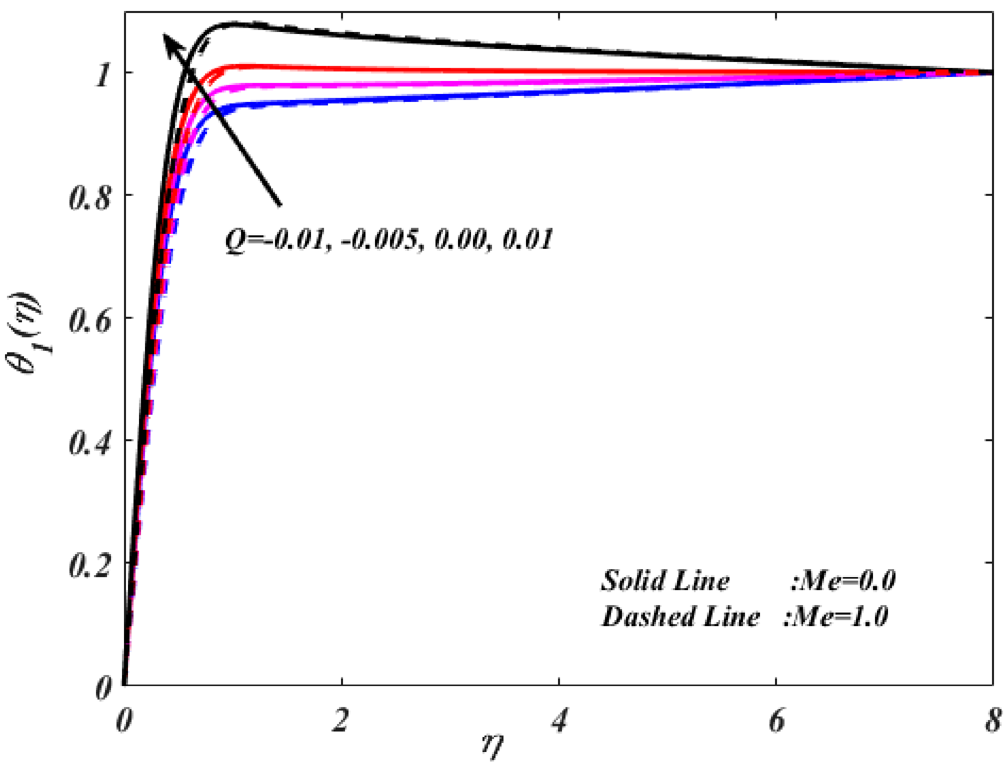

Figure 10. Effects of Q on $\theta_1(\eta)$.

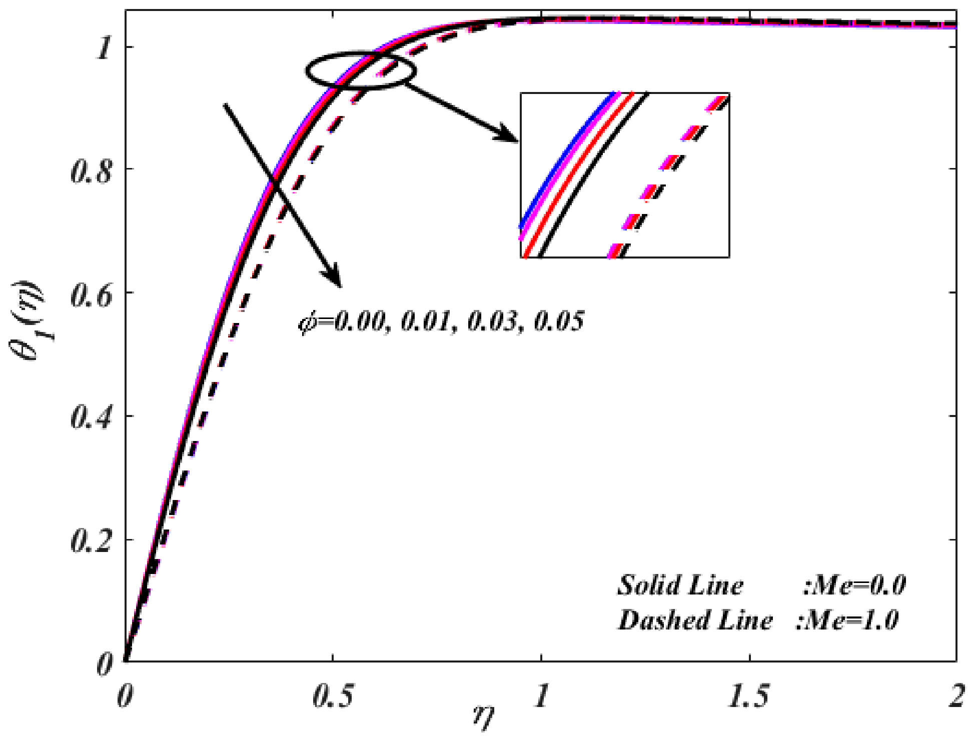

Figure 11. Effects of ϕ on $\theta_1(\eta)$.

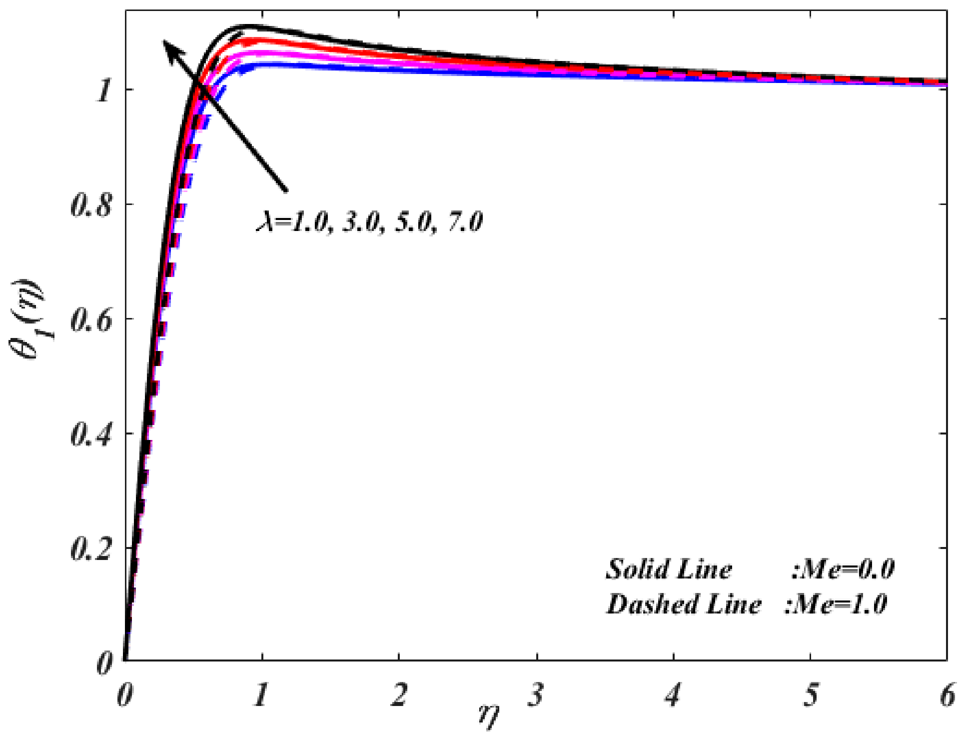

Figure 12. Effects of λ on $\theta_1(\eta)$.

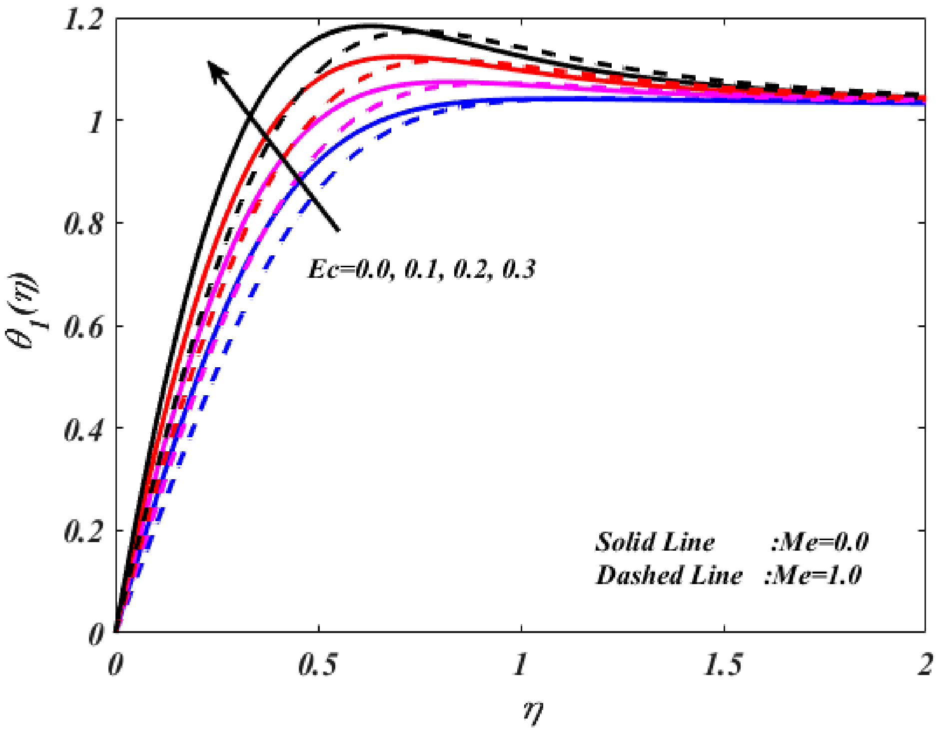

Figure 13. Effects of Ec on $\theta_1(\eta)$.

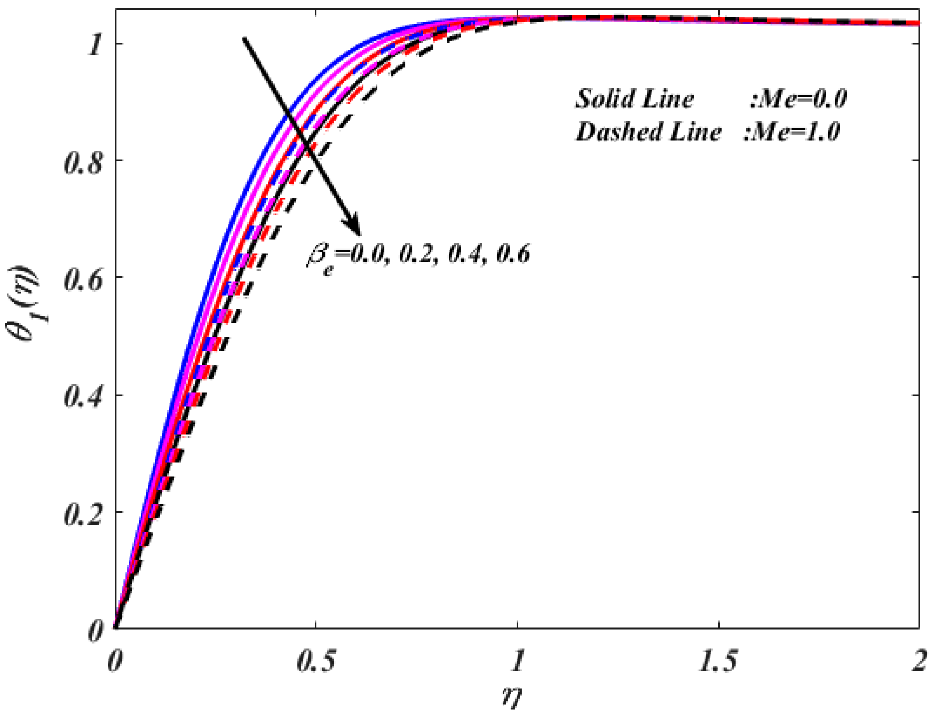

Figure 14. Effects of β_e on $\theta_1(\eta)$.

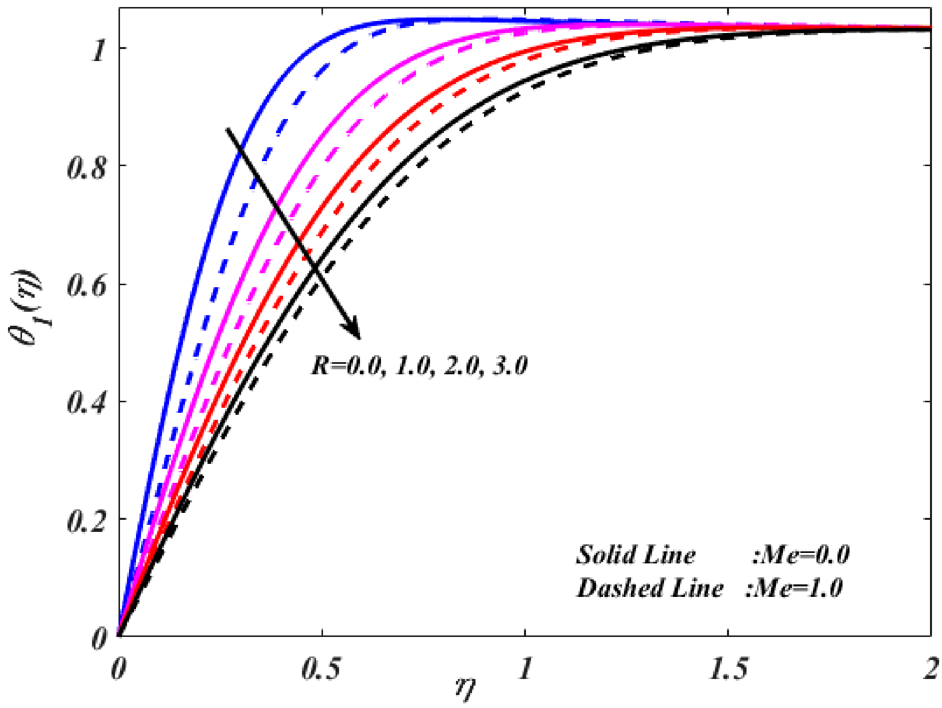

Figure 15. Effects of R on $\theta_1(\eta)$.

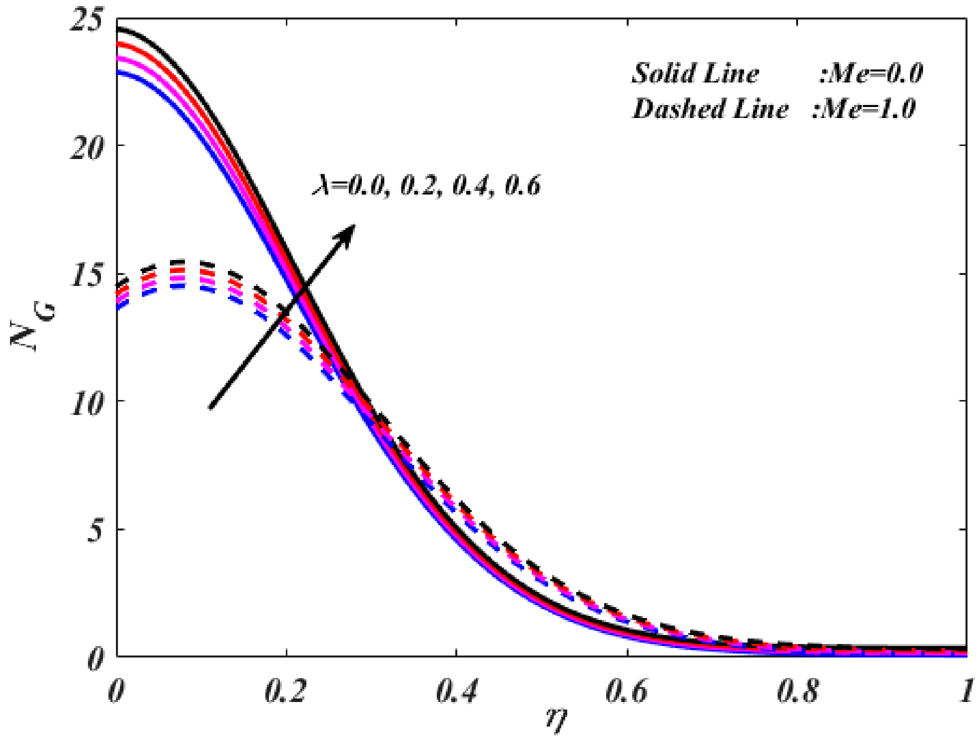

Figure 16. Effects of λ on N_G.

Figures 16–21 are plotted for investigating the significance of innumerable active features in the entropy generation (N_G) and Bejan number (Be). Figures 16 and 19 explore the effects of latent heat of the fluid parameter (λ) on (N_G) and (Be). It is noticed that improvement in (λ) enhances (N_G) and (Be). Figures 17 and 20 describe how the (N_G) and (Be) profiles are influenced by the variations in the fluid parameter $(\in)$. It is identified that improvement in (N_G) improves the values of the fluid parameter $(\in)$, and the opposite nature is observed for (Be). Physically, an increase in the values of the fluid parameters is observed as fluid velocity greatly increases and fluid viscosity significantly decreases. Figures 18 and 21 describe how the (N_G) and (Be) profiles are influenced by the variations in thermal radiation parameter (R). It is identified that improvement in (N_G) improves the values of the thermal radiation parameter (R), and the opposite nature is observed for (Be). Physically, the medium becomes more thermally diffusible as a result of thermal radiation.

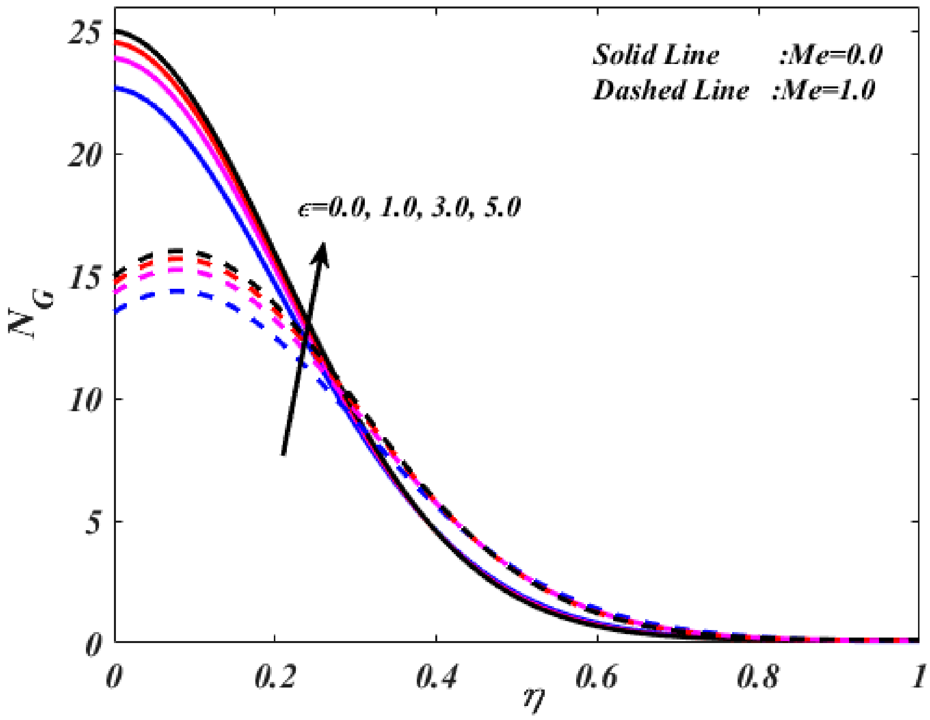

Figure 17. Effects of ε on N_G.

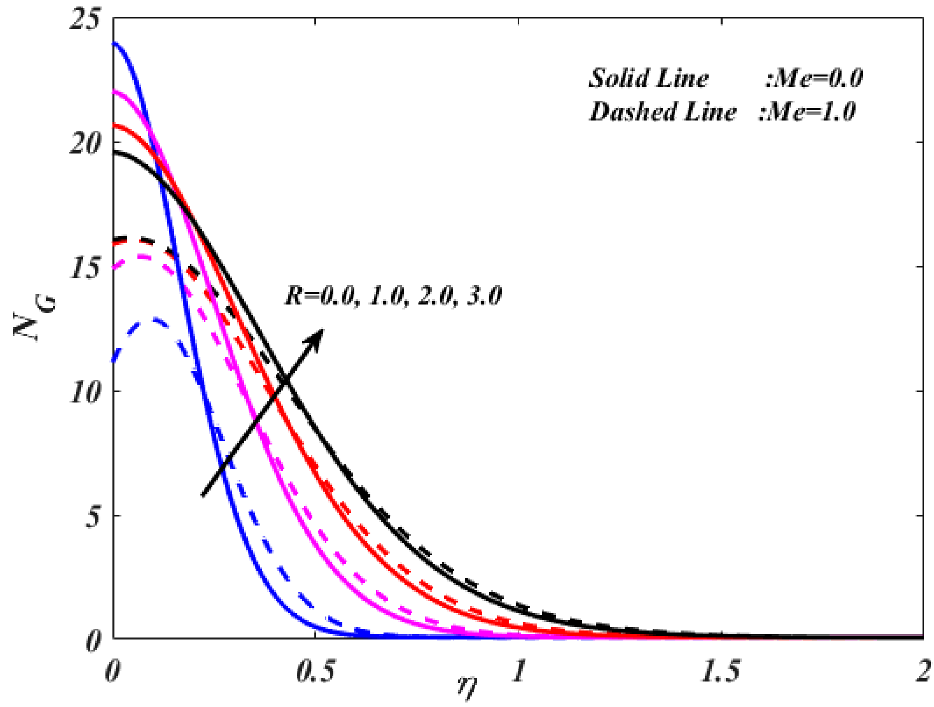

Figure 18. Effects of R on N_G.

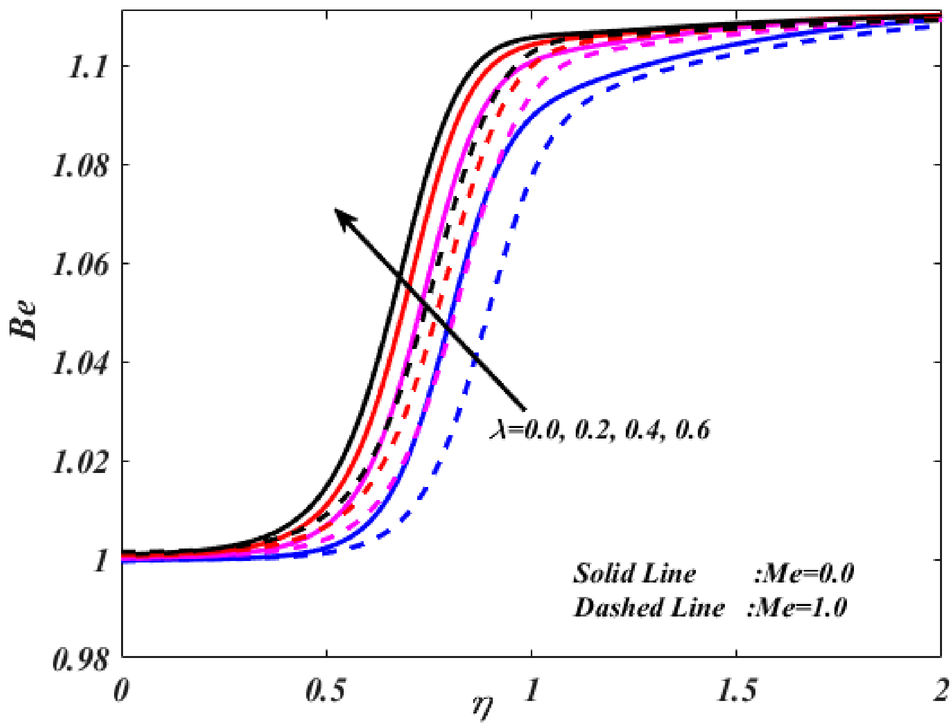

Figure 19. Effects of λ on Be.

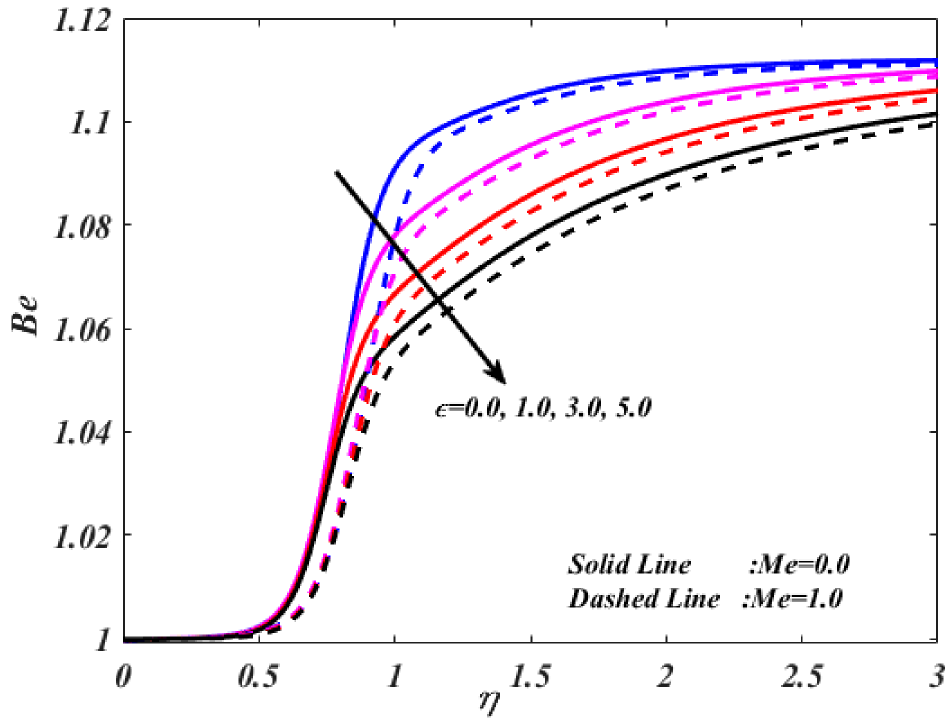

Figure 20. Effects of ε on Be.

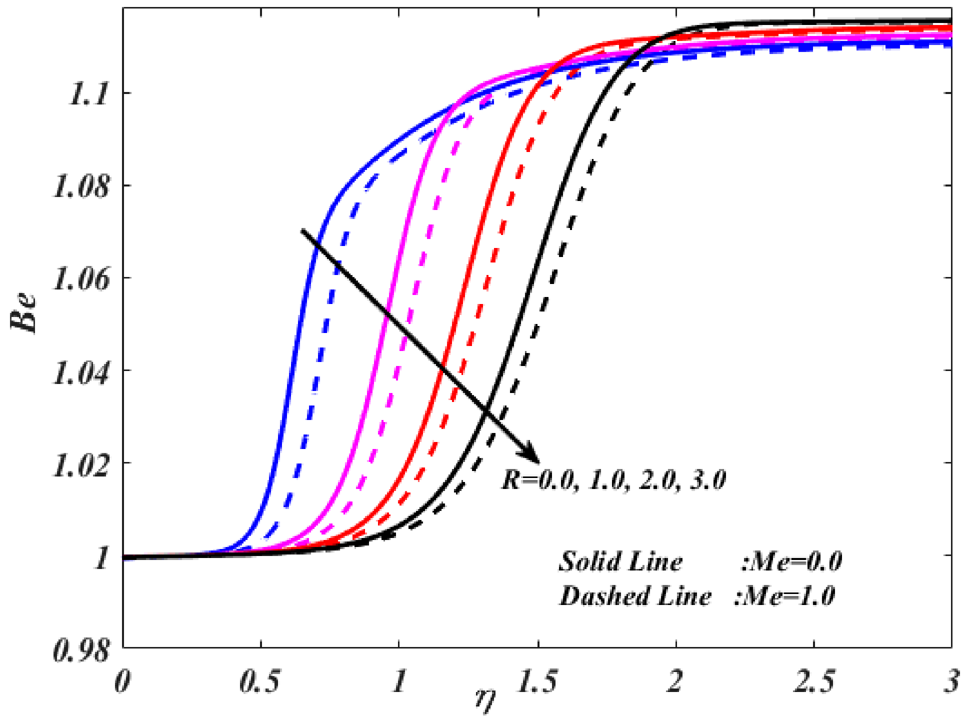

Figure 21. Effects of R on Be.

Figure 22 is outlined to reveal the influence of (Ec) and (Me) on $C_f\mathrm{Re}_x^{1/2}/2$. It is discovered that there is a slight decrease in the skin friction factor of the hybrid nanofluid over the sheet on the (Me) parameter. It is seen that $C_f\mathrm{Re}_x^{1/2}/2$ expands for developing values of (Ec). Figure 23 shows the effects of (Me) and $(\in)$ parameters on $C_f\mathrm{Re}_x^{1/2}/2$. It is recognized that the enlargement of the skin friction factor of the blood hybrid nanofluid at the surface amplifies $(\in)$. It is discovered that improving values of (Me) reduces the skin friction factor of blood hybrid nanofluid over the sheet. Figure 24 is outlined to reveal the influence of (Ec) and (Me) on $-Nu_x\mathrm{Re}_x^{-1/2}$. It is discovered that there is a decay in the Nusselt number of blood-based hybrid nanofluid over the sheet on the (Me) parameter. It is discovered that improving values of (Ec) decreases the Nusselt number of blood-based hybrid nanofluid over the sheet. Figure 25 is utilized to investigate the impact of ϕ and Me on the $-Nu_x\mathrm{Re}_x^{-1/2}$ of the blood nanofluid. The enhancement of the ϕ increments for the Nusselt number is evident, while conversely, a contrasting trend is observed for the Me. Figure 26 has been presented to illustrate the influence of Me and β_e on the value of $-Nu_x\mathrm{Re}_x^{-1/2}$. It is revealed that there is a less significant impact on the $-Nu_x\mathrm{Re}_x^{-1/2}$ of the hybrid nanofluid over the sheet on the (Me) parameter. It is seen that $-Nu_x\mathrm{Re}_x^{-1/2}$ increases for growing values of (β_e).

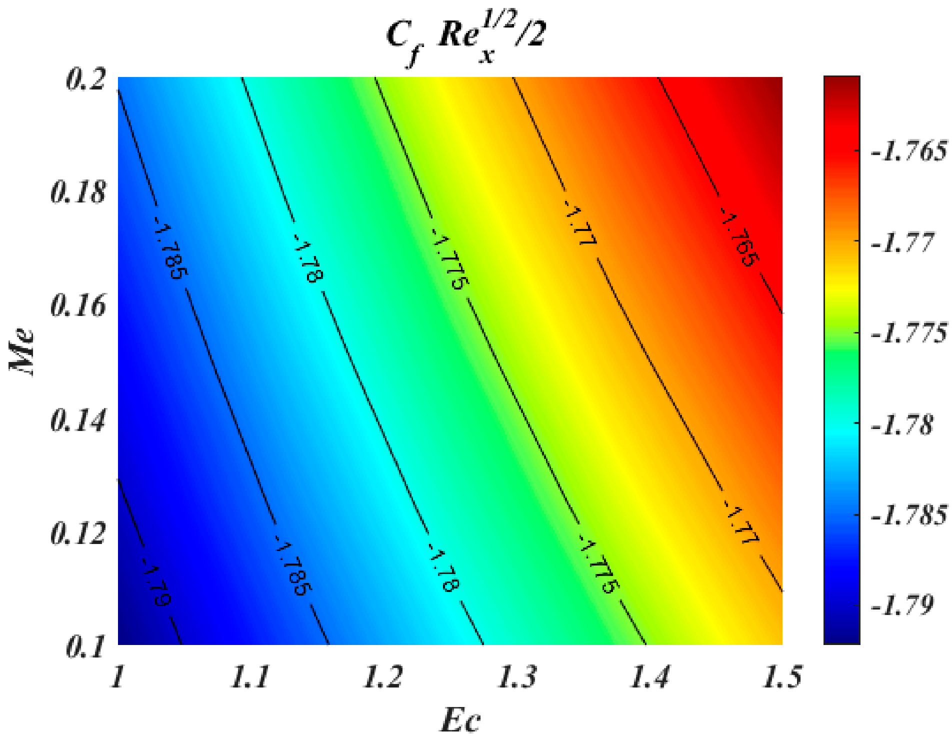

Figure 22. Effects of Me and Ec on $C_f\mathrm{Re}_x^{\frac{1}{2}}$.

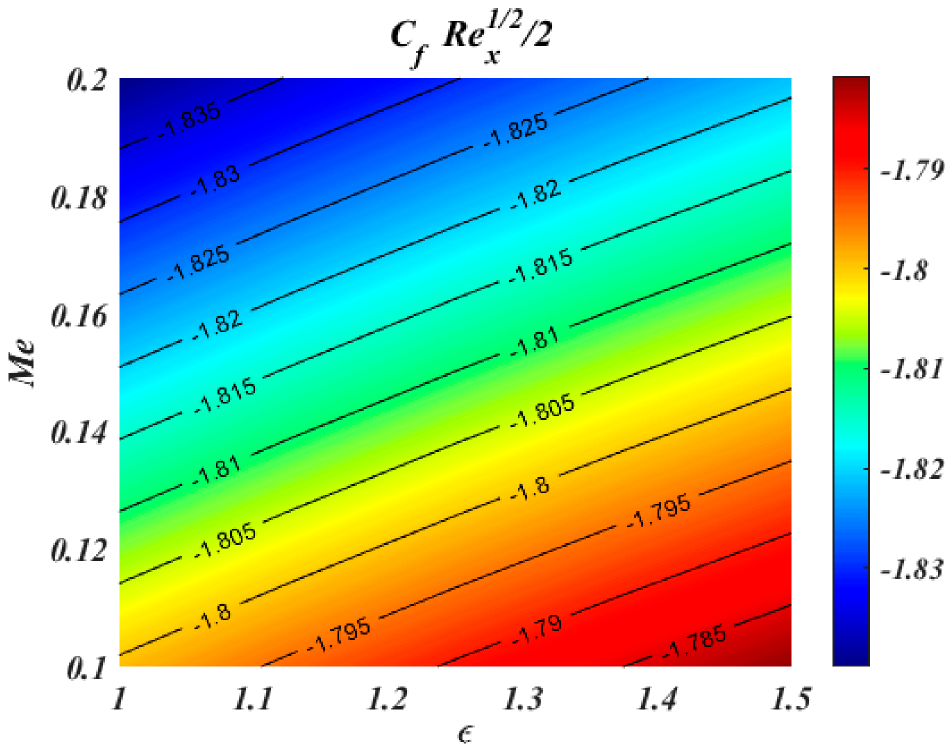

Figure 23. Effects of Me and ε on $C_f\mathrm{Re}_x^{\frac{1}{2}}$.

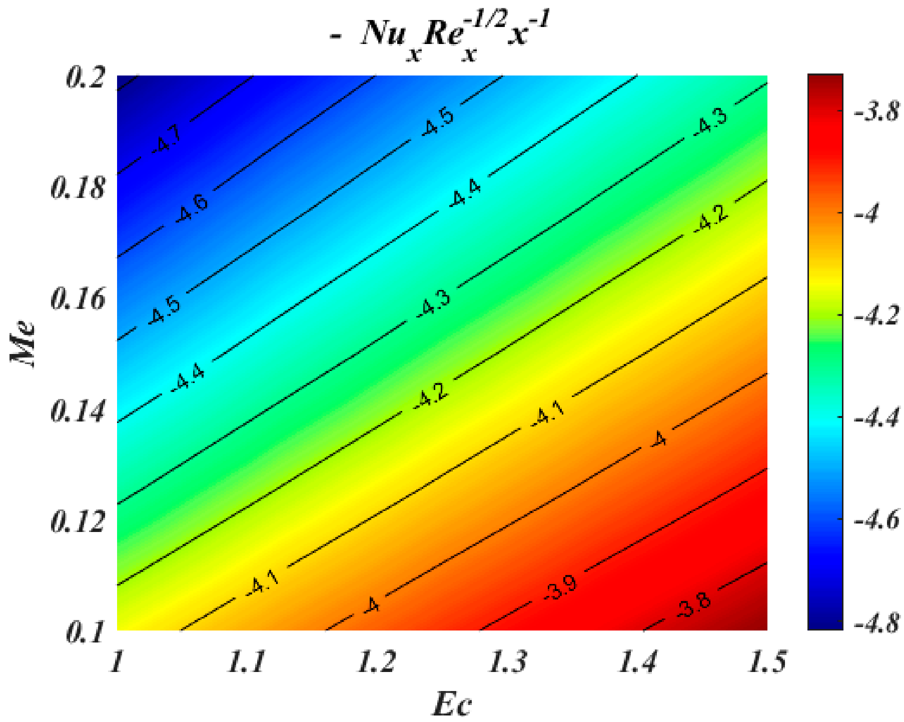

Figure 24. Effects of Me and Ec on $-Nu_x\mathrm{Re}_x^{-\frac{1}{2}}x^{-1}$.

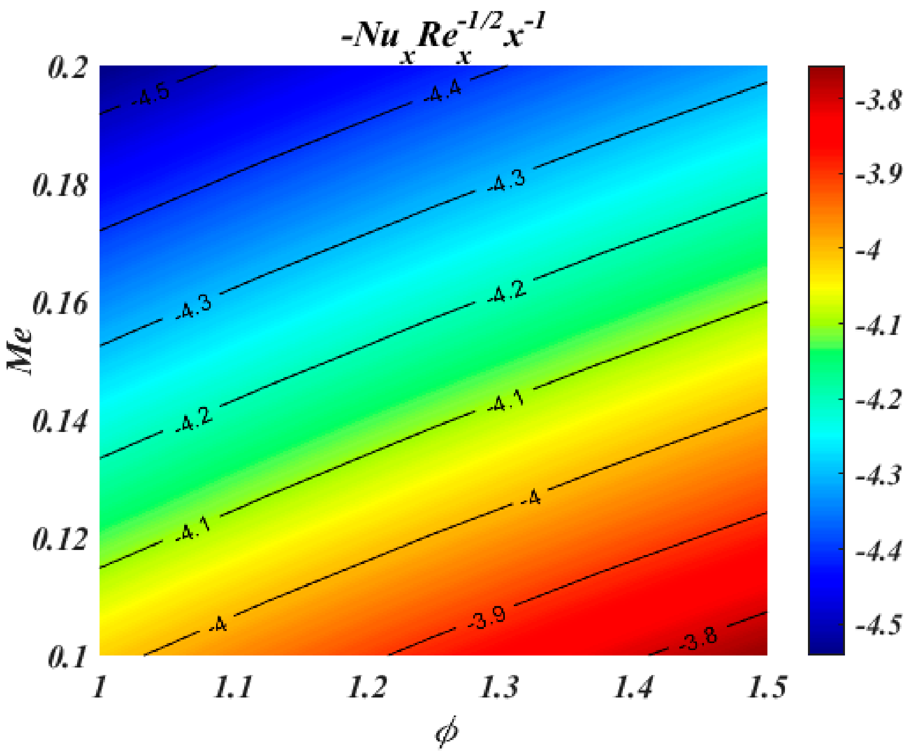

Figure 25. Effects of Me and ϕ on $-Nu_x\mathrm{Re}_x^{-\frac{1}{2}}x^{-1}$.

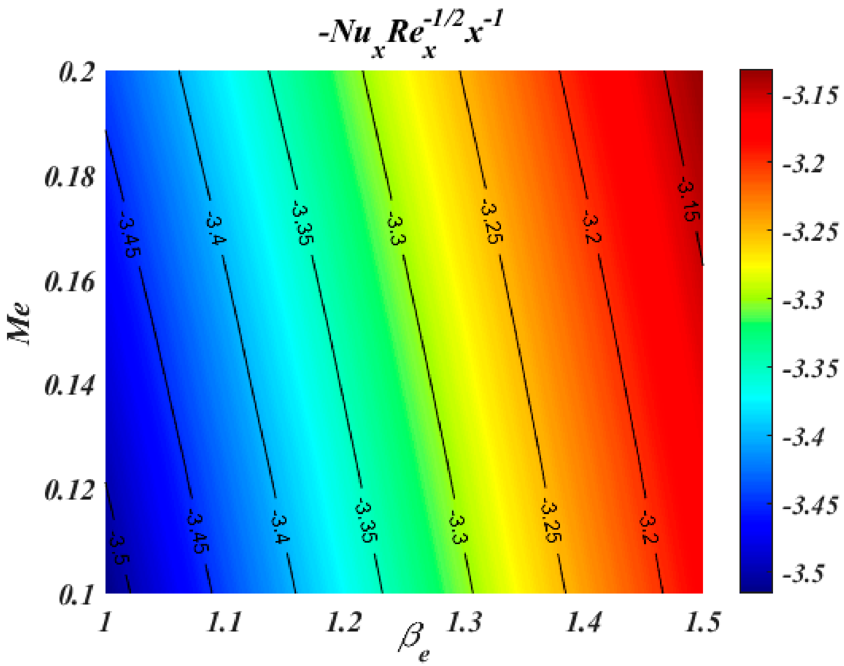

Figure 26. Effects of Me and β_e on $-Nu_x\mathrm{Re}_x^{-\frac{1}{2}}x^{-1}$.

7. Conclusions

This investigation aimed to analyze the entropy generation associated with the flow of a hybrid nanofluid, specifically Fe_3O_4-Au/blood, in a heat transfer scenario involving both melting and non-melting conditions. The study was conducted in the presence of a magnetic dipole over a permeable sheet, utilizing the Cattaneo–Christov heat flux model. It is important to note that the blood can be modeled as a Powell–Eyring fluid. The study presents a clear discussion of the physical effects of different momentum and thermal parameters through the use of graphical representations such as contour plots. The key findings of this examination are as follows:

- The artificial neural network model exhibits the advantageous properties of not necessitating linearization, exhibiting rapid convergence, and incurring a diminished processing cost.
- The velocity describes the rising nature by upgrading the fluid parameter.
- The temperature increased due to the boosting of the values of the Eckert number.
- The temperature decreased due to the boosting of the thermal relaxation parameter.
- The Nusselt number increased due to an improvement in the values of the nanoparticle volume fraction.
- The skin friction factor increases for growing values of the fluid parameter.
- Higher values of the radiation parameter enhance entropy generation and decrease the Bejan number.

Author Contributions: S.J. conceptualized the problem, S.R.R.R. completely solved and plotted the graphs, and H.T.B. and S.V.E. wrote the manuscript. All authors have read and agreed to the published version of the manuscript.

Funding: The author Shaik Jakeer thanks the Center for Computational Modeling, Chennai Institute of Technology, India, vide funding number CIT/CCM/2023/RP/017 for partially funding this work.

Data Availability Statement: Not applicable.

Conflicts of Interest: The authors declare that they have no known competing financial interests or personal relationships that could have appeared to influence the work reported in this paper.

Nomenclature:

M	magnetization (A/m)
T	temperature of the fluid (K)
$k\prime$	permeability of the porous medium
T_∞	temperature of the ambient fluid (K)
m_p	magnetic permeability
H	magnetic field
c_s	heat capacity of the solid surface (J/K)
Re_x	local Reynolds number
Q_0	heat generation/absorption coefficient
m_p	magnetic permeability
Me	melting parameter
c_p	specific heat at constant pressure ($\mathrm{Jkg}^{-1}\mathrm{K}^{-1}$)
K	the porosity parameter
k^*	mean absorption coefficient (m^{-1})
k	thermal conductivity
F^*	Forchheimer parameter
$Nu_x\mathrm{Re}_x^{-1/2}$	Nusselt number
$C_f\mathrm{Re}_x^{1/2}/2$	skin friction coefficient
u & v	velocity components (m/s)
x & y	Cartesian coordinates (m)
ε	dimensionless Curie temperature ratio
Q	heat source parameter
R	radiation parameter
Ec	Eckert number
Pr	Prandtl number
F_s	inertia coefficient
Greek symbols	
ρ	density ($\mathrm{kg\ m}^{-3}$)
ϕ	volume fraction of nanoparticle
α_1	temperature difference parameter
θ	dimensionless temperature
μ	dynamic viscosity ($\mathrm{kg\ m}^{-1}\ \mathrm{s}^{-1}$)
η	similarity variable
v	kinematic viscosity ($\mathrm{m}^2\mathrm{s}^{-1}$)
α	distance from origin to magnetic dipole
λ	latent heat of the fluid parameter
β_e	thermal relaxation parameter
β_f	ferromagnetic parameter
Subscripts	
f	fluid
bf	base fluid
hnf	hybrid nanofluid
Superscript	
$\prime$	differentiation with respect to η

References

1. Powell, R.E.; Eyring, H. Mechanisms for the relaxation theory of viscosity. *Nature* **1944**, *154*, 427–428. [CrossRef]
2. Asha, S.K.; Sunitha, G. Effect of joule heating and MHD on peristaltic blood flow of Eyring–Powell nanofluid in a non-uniform channel. *J. Taibah Univ. Sci.* **2019**, *13*, 155–168. [CrossRef]
3. Jafarimoghaddam, A. On the Homotopy Analysis Method (HAM) and Homotopy Perturbation Method (HPM) for a nonlinearly stretching sheet flow of Eyring-Powell fluids. *Eng. Sci. Technol. Int. J.* **2019**, *22*, 439–451. [CrossRef]
4. Patil, V.S.; Patil, A.B.; Ganesh, S.; Humane, P.P.; Patil, N.S. Unsteady MHD flow of a nano powell-eyring fluid near stagnation point past a convectively heated stretching sheet in the existence of chemical reaction with thermal radiation. *Mater. Today Proc.* **2021**, *44*, 3767–3776. [CrossRef]
5. Farooq, M.; Anjum, A.; Rehman, S.; Malik, M.Y. Entropy analysis in thermally stratified Powell-Eyring magnesium-blood nanofluid convection past a stretching surface. *Int. Commun. Heat Mass Transf.* **2022**, *138*, 106375. [CrossRef]

6. Bejan, A. A study of entropy generation in fundamental convective heat transfer. *J. Heat Transfer* **1979**, *101*, 718–725. [CrossRef]
7. Jakeer, S.; Reddy, P.B.A. Entropy generation on the variable magnetic field and magnetohydrodynamic stagnation point flow of Eyring–Powell hybrid dusty nanofluid: Solar thermal application. *Proc. Inst. Mech. Eng. Part C J. Mech. Eng. Sci.* **2022**, *236*, 7442–7455. [CrossRef]
8. Soomro, F.A.; Alamir, M.A.; El-Sapa, S.; Haq, R.U.; Soomro, M.A. Artificial neural network modeling of MHD slip-flow over a permeable stretching surface. *Arch. Appl. Mech.* **2022**, *92*, 2179–2189. [CrossRef]
9. Stephen, P.S. Low Viscosity Magnetic Fluid Obtained By the Culloidal Suspension of Magnetic Particles. U.S. Patent 3,215,572, 2 November 1965.
10. Hayat, T.; Rashid, M.; Imtiaz, M.; Alsaedi, A. Nanofluid flow due to rotating disk with variable thickness and homogeneous-heterogeneous reactions. *Int. J. Heat Mass Transf.* **2017**, *113*, 96–105. [CrossRef]
11. Badfar, H.; Motlagh, S.Y.; Sharifi, A. Study of blood flow inside the stenosis vessel under the effect of solenoid magnetic field using ferrohydrodynamics principles. *Eur. Phys. J. Plus* **2017**, *132*, 440. [CrossRef]
12. Nasir, S.; Sirisubtawee, S.; Juntharee, P.; Berrouk, A.S.; Mukhtar, S.; Gul, T. Heat transport study of ternary hybrid nanofluid flow under magnetic dipole together with nonlinear thermal radiation. *Appl. Nanosci.* **2022**, *12*, 2777–2788. [CrossRef]
13. Madhura, K.R.; Babitha; Iyengar, S.S. Impact of heat and mass transfer on mixed convective flow of nanofluid through porous medium. *Int. J. Appl. Comput. Math.* **2017**, *3*, 1361–1384. [CrossRef]
14. Madhura, K.R.; Atiwale, B.; Iyengar, S.S. Influence of nanoparticle shapes on natural convection flow with heat and mass transfer rates of fractional nanofluids. *Authorea Prepr.* **2020**, *46*, 8089–8105. [CrossRef]
15. Saleem, K.B.; Al-Kouz, W.; Chamkha, A. Numerical analysis of rarefied gaseous flows in a square partially heated two-sided wavy cavity with internal heat generation. *J. Therm. Anal. Calorim.* **2021**, *146*, 311–323. [CrossRef]
16. Kheioon, I.A.; Saleem, K.B.; Sultan, H.S. Analysis of natural convection and radiation from a solid rod under vacuum conditions with the aiding of ANFIS. *Exp. Tech.* **2023**, *47*, 139–152. [CrossRef]
17. Saleem, K.B.; Marafie, A.H.; Al-Farhany, K.; Hussam, W.K.; Sheard, G.J. Natural convection heat transfer in a nanofluid filled l-shaped enclosure with time-periodic temperature boundary and magnetic field. *Alex. Eng. J.* **2023**, *69*, 177–191. [CrossRef]
18. Keerthi, M.L.; Gireesha, B.J. Analysis of entropy generation in a fully wet porous moving longitudinal fin exposed to convection and radiation: Homogeneous and functionally graded materials. *J. Therm. Anal. Calorim.* **2023**, *148*, 6945–6957. [CrossRef]
19. Ali, B.; Siddique, I.; Khan, I.; Masood, B.; Hussain, S. Magnetic dipole and thermal radiation effects on hybrid base micropolar CNTs flow over a stretching sheet: Finite element method approach. *Results Phys.* **2021**, *25*, 104145. [CrossRef]
20. Padmavathi, R.; Dhruvathara, B.S.; Rashmi, K.; Ganesh Kumar, K. Two-phase hydromagnetic Eyring-Powell fluid flow over a stretching sheet suspended to a dusty particle. *Int. J. Model. Simul.* **2023**, 1–11. [CrossRef]
21. Javed, M.; Alderremy, A.A.; Farooq, M.; Anjum, A.; Ahmad, S.; Malik, M.Y. Analysis of activation energy and melting heat transfer in MHD flow with chemical reaction. *Eur. Phys. J. Plus* **2019**, *134*, 256. [CrossRef]
22. Nabwey, H.A.; Mahdy, A. Transient flow of micropolar dusty hybrid nanofluid loaded with Fe3O4-Ag nanoparticles through a porous stretching sheet. *Results Phys.* **2021**, *21*, 103777. [CrossRef]
23. Waqas, H.; Farooq, U.; Naseem, R.; Hussain, S.; Alghamdi, M. Impact of MHD radiative flow of hybrid nanofluid over a rotating disk. *Case Stud. Therm. Eng.* **2021**, *26*, 101015. [CrossRef]
24. Ishak, A.; Nazar, R.; Pop, I. Mixed convection on the stagnation point flow toward a vertical, continuously stretching sheet. *J. Heat Transfer* **2007**, *129*, 1087–1090. [CrossRef]
25. Pal, D. Buoyancy-driven radiative unsteady magnetohydrodynamic heat transfer over a stretching sheet with non-uniform heat source/sink. *J. Appl. Fluid Mech.* **2016**, *9*, 1997–2007. [CrossRef]